Second Generation of Non-Coupled Dinuclear Copper Sites Modeled in Azurin

A THESIS
SUBMITTED TO THE FACULTY OF THE GRADUATE SCHOOL
OF THE UNIVERSITY OF MINNESOTA
BY

Erika Lee Bladholm

IN PARTIAL FULFILLMENT OF THE REQUIREMENTS
FOR THE DEGREE OF
MASTER OF SCIENCE

Steven M. Berry

May 2011

Acknowledgements

The progress I have made on these projects would not have been possible without the support and guidance Dr. Steven Berry has provided over the last two years. Additionally, much of the work completed on these projects before I joined the lab was carried out by Sasha Kniazieva, Nick Zehm, and Madelyn Baker. There were also two undergraduate researchers, Andy McCabe and Greg Reynolds, who were instrumental in helping me carry out this research.

Abstract

Protein design is a rapidly developing field of biological chemistry. Our approach to protein design involves layering structural components which are thought to be important for function onto a protein scaffold. In this way, we are uniquely able to individually test each layer for gain-of-function, as opposed to typical mutagenesis studies which look for loss-of-function. Elucidating structure and function relationships for copper proteins through protein design may ultimately lead to the design of industrial catalysts, inhibitors, or a further understanding of current biological pathways. Nitrite reductase (NiR) and peptidyl glycine α-hydroxylating monooxygenase (PHM) both use non-coupled dinuclear copper sites to catalyze biologically relevant reactions; however mechanistic details of these enzymes are not fully understood. Azurin was chosen as a protein scaffold to model these non-coupled dinuclear copper sites due to its stability, high purification yields, and existing structural similarities to these enzymes. Azurin has an existing type one (T1) electron transfer copper site. A second copper binding site was incorporated to create the first generation models of these enzymes in azurin. These first generation models have shown catalytic activity but remain much less active than the native form. The catalyzed reactions require the transfer of an electron from a T1 copper site to the spectroscopically non-coupled type two (T2) copper catalytic site. Better facilitation of the electron transfer between these two sites is hypothesized to increase the activity in our models. Three second generation variants were created to facilitate electron transfer, as well as to provide insight into fundamental structure function relationships.

Table of Contents

List of Tables

List of Figures

ABBREVIATIONS

T1	Type 1 Copper Protein Site Classification (Functions in Electron Transfer)
T2	Type 2 Copper Protein Site Classification (Functions in Catalysis)
WT	Wild Type
NiR	Nitrite Reductase
PHM	Peptidyl Glycine α-Hydroxylating Monooxygenase
TBM	Tyramine β-monooxygenase
EPR	Electron Paramagnetic Resonance
IPTG	Isopropyl β-D-1-thiogalactopyranoside
LMCT	Ligand to Metal Charge Transfer
Tris	tris(hydroxymethyl)aminomethane
OAc	Acetate

Amino Acid 3 Letter Abbreviations Used

Asn	Asparagine	His	Histidine	Trp	Tryptophan
Asp	Aspartic acid	Lys	Lysine	Tyr	Tyrosine
Cys	Cysteine	Met	Methionine	Val	Valine
Gln	Glutamine	Phe	Phenylalanine		
Gly	Glycine	Pro	Proline		

Flow chart illustrates the models created using azurin as a scaffold

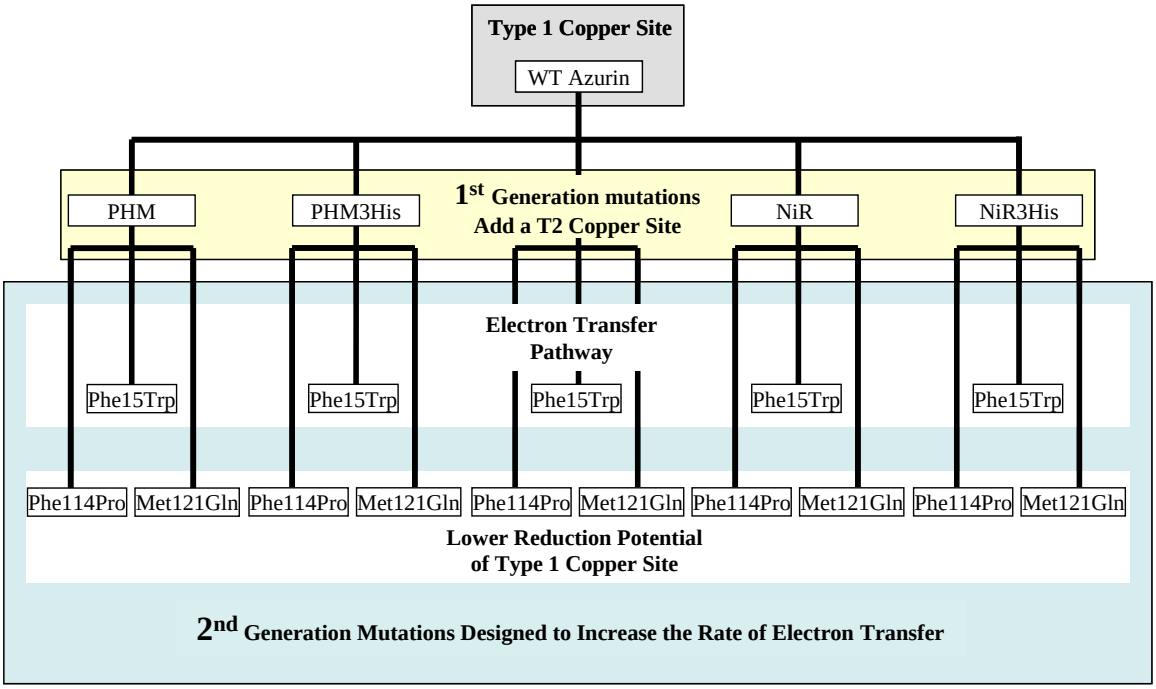

CHAPTER 1
NONCOUPLED DINUCLEAR COPPER SITES OF NITRITE REDUCTASE MODELED IN AZURIN

1.1 Introduction

1.1.1 The Role of Nitrite Reductase in the Nitrogen Cycle

The nitrogen cycle is of particular interest due to its close relationship with agriculture and climate change. Humans are changing the cycle by burning fossil fuels and increasing nitrogen sources in the soil from fertilizers.[1] The gases emitted from burning fossil fuels are some of the same gases the bacteria involved in denitrification release as a product of respiration. Some of these gases are greenhouse gases, contribute to acid rain, or have been linked to ozone depletion.[1-4] The bacteria involved in denitrification use various nitrogen oxyanions rather than dioxygen as terminal acceptors of electron transport.[3]

The nitrogen cycle (shown in Figure 1) is carried out primarily by microorganisms and is a cycle consisting of three major processes: denitrification, nitrification, and nitrogen fixation.[3] Dinitrogen gas (N_2) from the atmosphere is reduced to ammonium (NH_4^+) in a process called nitrogen fixation.[3] The nitrogen fixing microorganisms use ferredoxins or flavin-containing electron transfer proteins as electron donors; however, the activation energy required to complete these reactions comes from the hydrolysis of 16 equivalents of ATP for each N_2 fixed.[5] Another source of organic nitrogen in the soil comes from the decomposition of plants, animals and waste, which may be used for biosynthesis.[3]

The second process in the nitrogen cycle is nitrification which is the oxidation of ammonium to nitrate (NO_3^-).[3] This oxidation is completed by a bacterial class known as nitrifers and provides nitrate in the soil for plant metabolism.[3, 5] The reduction of nitrate to ammonia is the reverse of nitrification, known as ammonification or nitrate assimilation and is carried out by bacteria, fungi and plants.[3, 5]

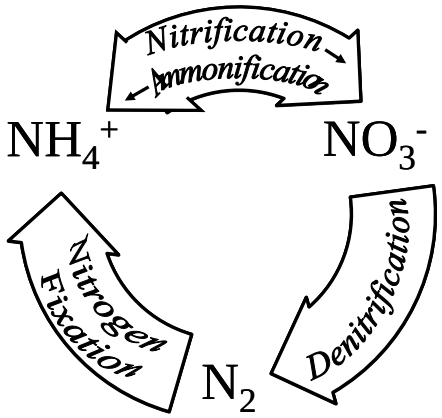

Figure 1: The nitrogen cycle is carried out primarily by microorganisms and is a cycle consisting of three major processes: denitrification, nitrification, and nitrogen fixation.

Denitrification is the reduction of nitrate to dinitrogen gas.[3] The process of denitrification decreases the available nitrate in soil. There are four major metal binding proteins involved in sequentially decreasing the oxidation state of nitrogen which are shown in Figure 2.[6] The metals involved (molybdenum (Mo), Heme (Fe), coupled dinuclear copper sites (Cu-Cu), and non-coupled dinuclear copper sites (T1Cu T2Cu)) are shown in Figure 2 along with the oxidoreductase that coordinate each. In bacterial denitrification, nitrate is transported to the cytoplasm where the reduced membrane bound nitrate reductase (NaR-Mo^{+4}) donates two electrons for the reduction of nitrate to nitrite.[7] Nitrite reductase (NiR) is a non-coupled dinuclear protein which catalyzes the

first committed step in denitrification.[4] In the periplasm, NiR is reduced by either azurin or cytochrome c_{551} (which acts as a mediator between azurin and NiR).[8] Nitrite is transported to the periplasm where NiR reduces it to nitric oxide.[6] Nitric oxide is reduced to nitrous oxide by nitric oxide reductase (NOR) which is then reduced to dinitrogen by nitrous oxide reductase (N_2OR).[6]

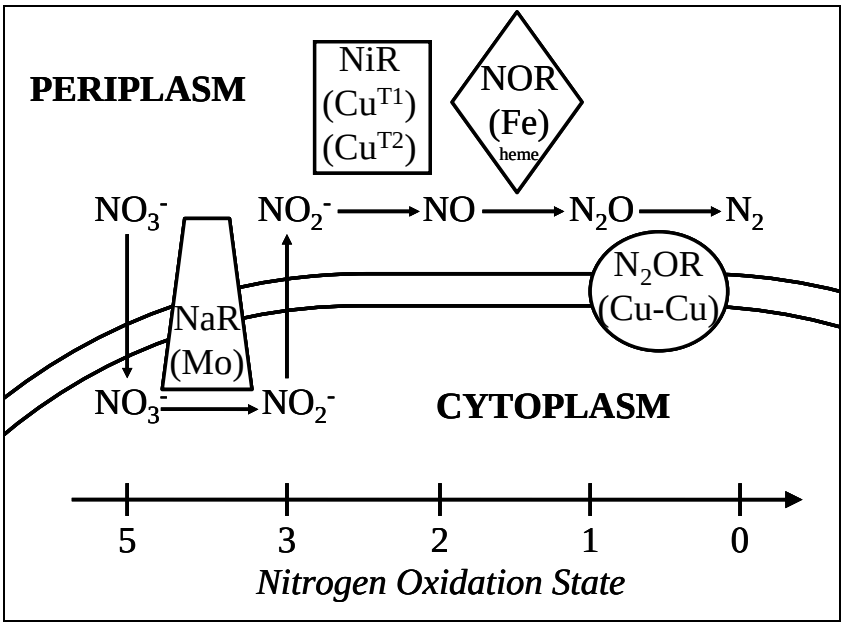

Figure 2: Bacterial Denitrification Pathway uses four metal binding proteins to catalyze the reduction of nitrate to dinitrogen gas.

Denitrification releases nitric oxide and nitrous oxide which as previously mentioned is harmful to the environment. The release of these gases also depletes soil of nitrate which is required for plant metabolism and is thus an undesirable process for agriculture.

1.1.2 Native Nitrite Reductase

Nitrite reductase (NiR) is a biologically relevant bacterial enzyme which catalyzes the reduction of nitrite to nitric oxide in denitrification.[3] There are several isoforms of nitrite reductase including an iron binding NiR and both green and blue copper NiR. The focus of this research is on the blue copper nitrite reductase which contains a type one (T1) copper site functioning as the electron transfer site.[9] The catalytic site is characterized as a type two (T2) copper site which binds nitrite, accepts an electron from the T1 copper site, and catalyzes the reduction of nitrite.[9] The order of electron transfer and substrate binding has been the subject of debate. Either nitrite binds to the already reduced T2 site, or nitrite may bind to the oxidized T2 copper before an electron from the T1 copper is donated.[10]

Much has been learned about the NiR mechanism through synthetic modeling. A variety of nitrite binding modes have been observed with T2 copper models. Nitrite has been shown to bind the reduced form of the T2 copper models end-on through the nitrogen atom, as opposed to the oxidized T2 copper model where nitrite binds in a bidentate fashion (side-on) through both oxygen atoms.[11-14] Characterization of these models with X-ray crystallography and kinetics studies support that nitrite preferentially binds the oxidized form of the synthetic T2 copper model.[11, 12, 14] Recent protein crystal structures of substrate bound to native NiR and density functional theory calculations also support the side-on coordination of nitrite to T2 Cu^{+2} versus end coordination through nitrogen to the reduced copper site.[4, 10, 13] A mechanism (represented by Figure 3) was derived from the combined knowledge of the synthetic models and the native enzyme.[14]

This mechanism proposes that nitrite binds to T2 Cu^{+2} (Figure 3a), prior to accepting an electron from the T1 copper site (Figure 3b).[14] Upon this reduction to T2 Cu^{+}, nitrite rearranges to bind copper end-on through the nitrogen atom (Figure 3c).[14] This rearrangement appropriately places one of the oxygen atoms from nitrite in close proximity to a hydrogen bonding network formed by Asp and His which provide the two protons required for catalysis (Figure 3d).[14] At this point, copper donates one electron to nitrite, and the electrons which form the nitrogen-oxygen bond are donated to protons in the hydrogen bonding network to form water (Figure 3e).[14] Nitric oxide is released and water is left coordinating T2 Cu^{+2} after a proton restores the hydrogen bonding network (Figure 3f).[14]

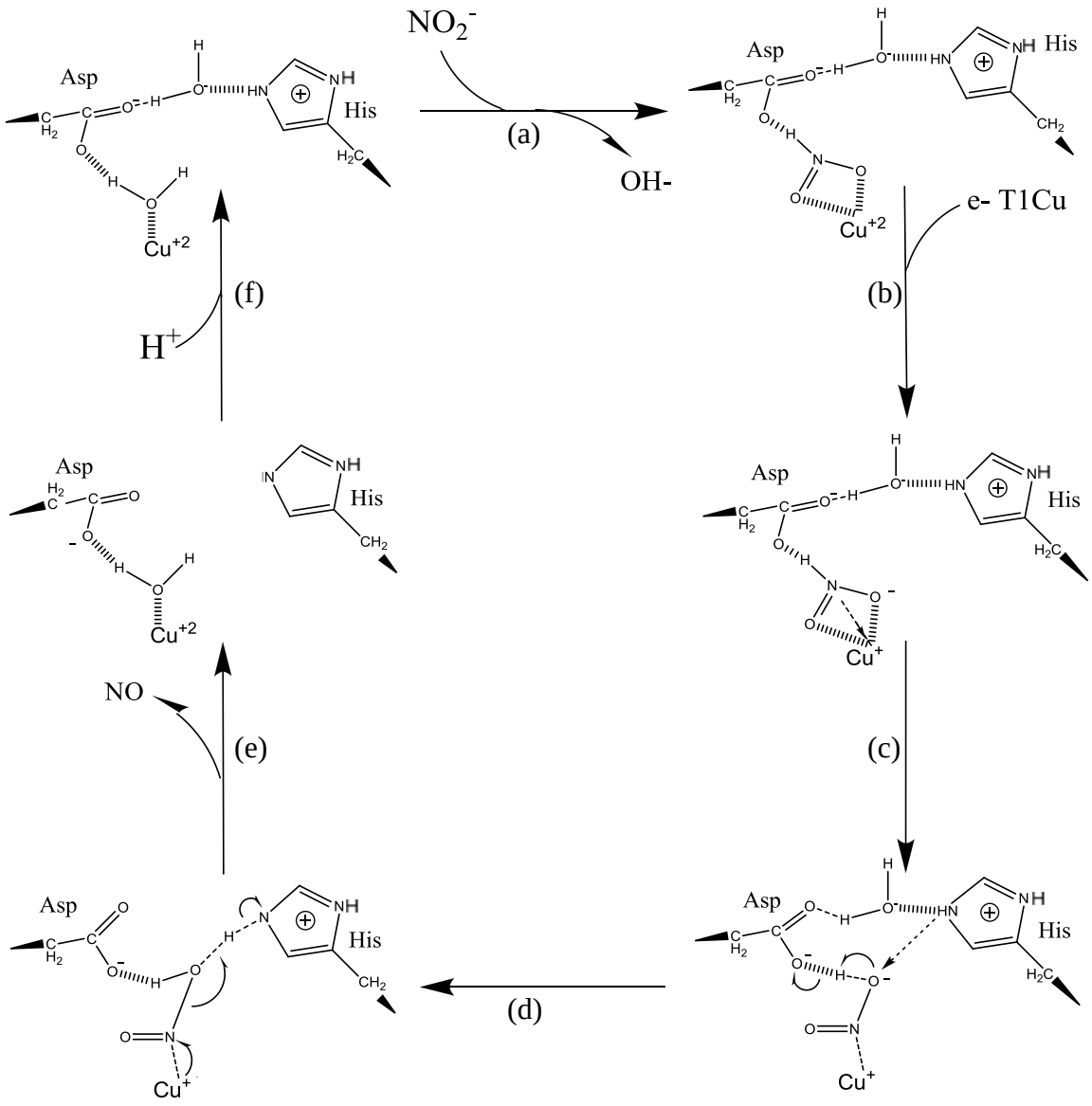

Figure 3: A mechanism for nitrite reductase was derived from the combined knowledge of the synthetic models and the native enzyme.[14] The side – on coordination of nitrite to oxidized copper is shown in (a) – (b), while the end-on coordination of nitrite is shown in (c) – (d). The nitric oxide product is released in (e) and the enzyme is restored to its initial resting state upon protonation in (f).[14]

1.1.3 First Generation Models of NiR Utilize Azurin as a Scaffold

A number of synthetic copper complexes have been designed to model these enzymes and have shed light on the roles of the coordinating residues, the catalytically active species, as well as the plausible reaction intermediates.[12] Using azurin as a protein scaffold distinguishes it from the previous synthetic models.

Azurin has a T1 copper site (circled in Figure 4b), similar to the T1 copper site in NiR (circled in Figure 4a).[9] The azurin copper site is characterized by the narrow copper hyperfine coupling constant in the parallel region of the electron paramagnetic resonance (EPR) spectrum.[7] No other copper sites exist in azurin; however there is a β-sheet motif similar to NiR, making azurin ideal for the design of a second copper site.[9]

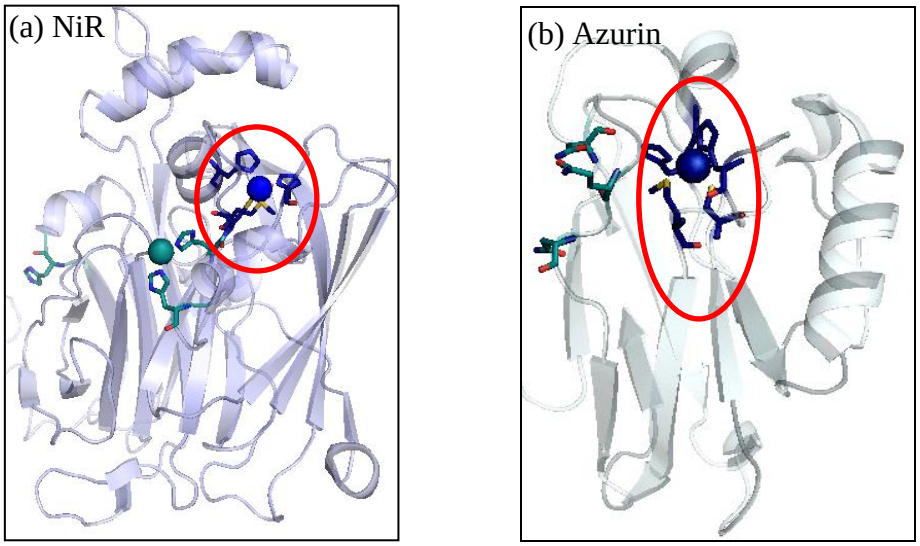

Figure 4: Structural comparisons of one monomer of native nitrite reductase and native azurin are shown with the type one copper site circled for each.
(a) Nitrite Reductase PDB ID: 2Y1A rendered in Pymol 1.10
(b) Azurin PDB ID: 4AZU rendered in Pymol 1.10

Azurin is a small (14 kDa) bacterial protein which functions as an electron donor in the electron transport chain.[15] The blue copper nitrite reductase is composed of three

35 kDa monomers which form a 105 kDa homotrimer.[16] About one third of each monomer's surface area interacts with adjacent monomers to stabilize the homotrimer.[4] Similar to azurin, each monomer of nitrite reductase also has a blue T1 copper electron transfer site (circled in Figure 4a). The β-barrel Greek key motif surrounding both the T1 copper centers is characteristic of the oxidoreductase class of enzymes.[9] Structural similarities, smaller size, higher purification yields and stability make azurin an ideal scaffold for modeling NiR.

The T1 copper site in both NiR (Figure 5a) and azurin (Figure 5b) is coordinated tightly by 3 ligands (His_2Cys) and by 2 weak axial ligands (Met, backbone carbonyl).

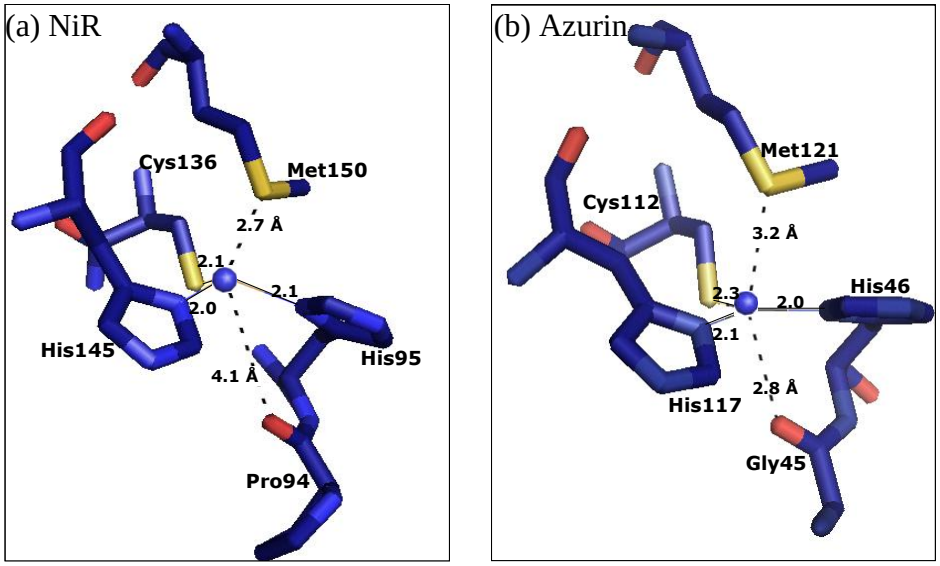

Figure 5: Type one copper site of (a) native blue copper NiR PDB ID: 2VN3 and (b) wild type azurin PDB ID: 4AZU

The three planar ligands coordinate through the nitrogen atoms of His117 and His46 and through the sulfur atom of Cys112. The strong cysteine to copper ligand interaction has covalent character resulting from the overlap between the p-orbital of

sulfur with the d_{x2-y2} copper orbital.[17, 18] There are also two weak axial ligands. The axial methionine sulfur coordinates stronger in NiR than in azurin, and the backbone carbonyl axial ligand is weaker in NiR. Both T1 sites have characteristic T1 copper function and spectroscopy (refer to Tables 1 – 4 for details).

Native nitrite reductase also has a T2 copper site coordinated by three histidines. Two of these histidines (His100 and His135) belong to the same monomer as the T1 copper site and the third histidine (His306) coordinates from an adjacent monomer.[19] A distant aspartic acid (Asp98) is thought to assist in substrate binding and catalysis as shown by the mechanism in Figure 3.[9, 19]

Two models were created to model native NiR and were named Az→NiR and Az→NiR3His. The T1 site was conserved in azurin to create both NiR models, and a T2 copper site was incorporated on the antiparallel β – strands 5 and 8 of wild type (WT) azurin. Quikchange mutagenesis was used to incorporate the mutations Asp10His, Gln14His, and Asp16His which were designed to mimic the T2 site of native NiR in the variant called Az→NiR3His (native NiR in Figure 6a is compared to the Pymol predicted structure of Az→NiR3His in Figure 6b).[9]

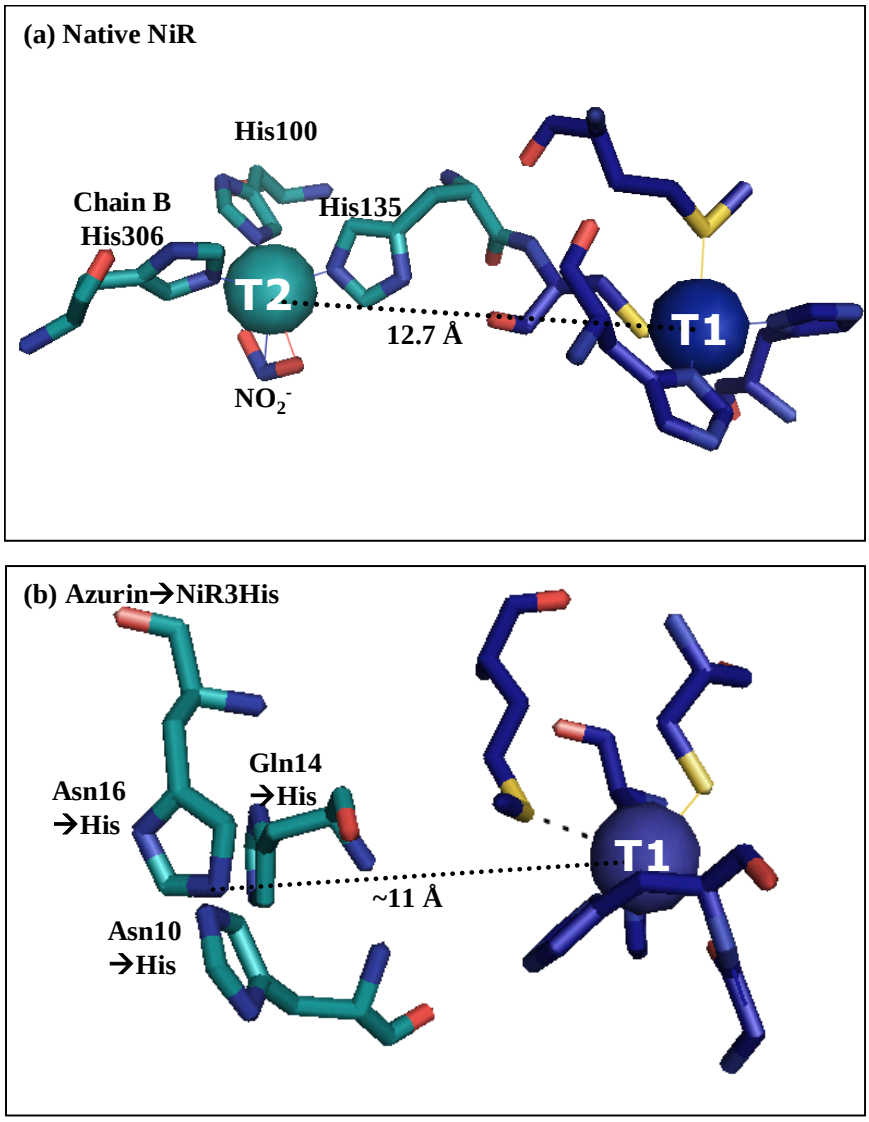

Figure 6: Structural comparison between (a) the T2 site in native NiR PDB ID: 1NDT and (b) the Pymol predicted structure of Az→NiR3His

The Az→NiR variant was similarly created except that Gln14 was changed to Asp rather than His to model the distant aspartic acid in native NiR which is thought to assist in substrate binding and catalysis.[19] Spectroscopic characterization of these models indicated that the Az→NiR3His variant is a good spectroscopic model for native NiR; however, the Az→NiR variant was dissimilar.[9] In addition to being a good spectroscopic

model, the activity assays indicated the Az→NiR3His variant also has nitrite reductase activity. The Az→NiR model also had activity, but was not as active as the Az→NiR3His model. This is most likely a result of weaker copper binding and the lack of the third coordinating histidine.[9] Both of these first generation models are less active than native NiR, so the opportunity to improve the activity of our models was taken advantage of by creating a second generation of models.

1.1.4 Second Generation Models of Nitrite Reductase

Three mutations (Phe114Pro, Met121Gln, and Phe15Trp) individually layered onto five existing first generation azurin variants (WT-Az, Az→PHM, Az→PHM3His, Az→NiR, and Az→NiR3His) are hypothesized to increase the electron transfer rate and thus the activity of each model. For simplicity, this chapter will focus on these second generation mutations layered on the most catalytically active model Az→NiR3His. The rate of electron transfer is dependent on both kinetic (electronic coupling between the initial and final states (H_{AB})) and thermodynamic (Gibbs free energy (ΔG) and the reorganization energy (λ)) components.[20] The potential difference between the two non-coupled copper sites contributes to the thermodynamic component. The first two second generation variants (Phe114Pro and Met121Gln described in detail below) aim to reduce the reduction potential of the T1 site in wild type azurin (previously measured at 357 ± 5 mV) to bring it closer to the potential of the T2 copper, as is seen in native NiR.[21] The reduction potential of the T1 site of native NiR has been measured at 255 ± 3 mV, and the T2 site is 244 ± 18 mV.[22] The first generation Az→NiR3His variant is a good spectroscopic model of native nitrite reductase, so it is likely the T2 site of our model has a similar reduction potential; however we have not yet measured this. The third variant (Phe15Trp is described below) aims to address the kinetic component by creating a more efficient physical pathway for the electron to travel from the T1 site to the T2 site.

The Phe114Pro mutation has previously been shown to reduce the potential of wild type azurin by 90 mV in Tris buffer at pH 8.[23, 24] The crystal structure of this variant shows that the mutation causes the type one copper to come out of the plane bringing

copper closer to Met121 (represented by the arrow in a Pymol predicted structure in Figure 7) as a result of the proline sterically hindering the axial coordination of the backbone carbonyl from Gly45.[24] Similarly, copper is slightly out of the plane created by His_2Cys in native NiR and the distance between the axial backbone carbonyl is much greater than for the other ligands (refer to Figure 5 for native NiR).

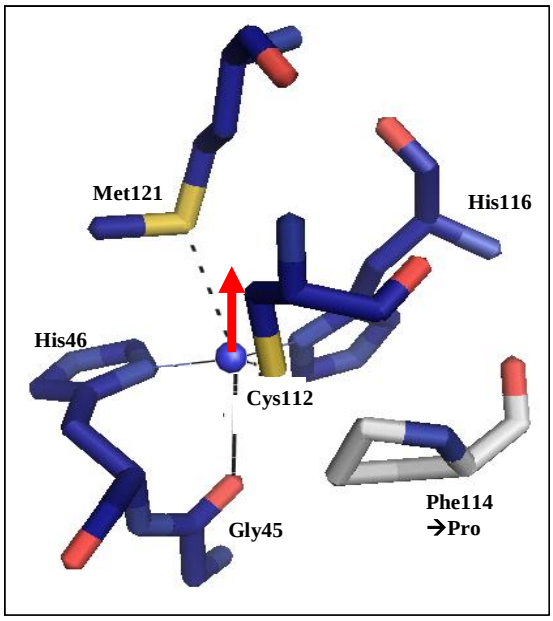

Figure 7: Azurin T1 site with Pymol predicted Phe114Pro mutagenesis: The arrow indicates the displacement of copper observed in the crystal structure from the literature as a result of this mutation.[24]

Tables 1 and 2 compare the literature reported spectroscopic properties of azurin Phe114Pro with native NiR. The EPR and UV-visible absorption properties of native NiR are closer to those of the Phe114Pro azurin mutant than they are for wild type azurin. It is hypothesized that layering the Phe114Pro mutation onto the first generation Az→NiR3His variant will increase the NiR activity. This hypothesis stems from creating more thermodynamically favored electron transfer between the two copper sites, as well

as from the additional structural similarities between the Phe114Pro azurin mutant and native NiR's T1 sites.

Table 1: UV- visible absorption properties reported in the literature are compared between wild type azurin, native nitrite reductase and the azurin Phe114Pro variant

T1 Cu(II)	$S(\pi) \rightarrow Cu(d_{x^2-y^2})$ **λ nm**	**ε $M^{-1}cm^{-1}$**
WT-Azurin[24]	628	5100
Native NiR[16]	595	-
Azurin Phe114Pro [24]	599	4300

Table 2: EPR properties reported in the literature are compared between wild type azurin, native nitrite reductase and the azurin Phe114Pro variant

T1 Cu(II)	A_z	A_x	A_y	g_z	g_x	g_y
WT-Azurin[24]	53	14	14	2.261	2.035	2.054
Native NiR[16]	63	-	-	2.24	2.05	2.05
Azurin Phe114Pro [24]	64	13	11	2.209	2.04	2.046

The second mutation designed to decrease the reduction potential of the T1 copper site in our first generation model is Met121Gln. The Met121Gln mutation has also been previously characterized in wild type azurin and was shown to decrease the reduction potential of the T1 copper site by 100 mV in phosphate buffer at pH 7.0.[23, 25] The oxygen atom from Gln which replaces the S from Met is one carbon bond length closer to copper than S_{Met}. Oxygen and Cu(II) are both hard atoms, while the sulfur from Met is soft; therefore hard / soft ligand chemistry supports that oxygen is a better ligand

for Cu(II) than sulfur. Also, Cu(II) is harder than Cu(I) so a hard oxygen ligand would favor the oxidized state. Copper would be more likely to give up an electron thus decreasing its reduction potential, when additional electron density donated from O_{Gln} is closer to copper due to repulsions. As a result, the crystal structure shows that copper sinks down lower past the planar ligands as shown by the arrow in Figure 8.

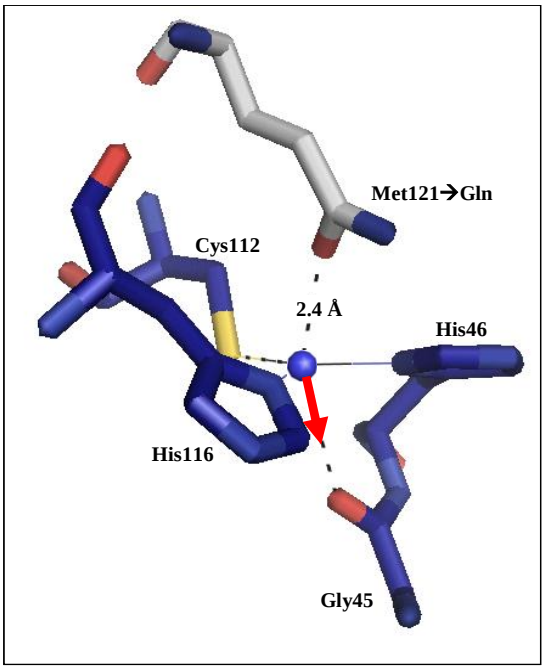

Figure 8: Azurin T1 site is shown with the Met121Gln mutation as predicted by Pymol. The arrow indicates the displacement of copper observed in the crystal structure from the literature as a result of this mutation.[25]

More structural details of Az→NiR3His→Met121Gln are discussed in section **1.3.2(b)** of the spectroscopic results; however comparison of the known UV-visible absorption and EPR properties are compared in Tables 3 and 4 respectively.[16, 25] Differences in the pH and buffer conditions may result in slight changes in LMCT bands

and variation of the EPR parameters so they have also been included. The parameters listed in Tables 3 and 4 differ slightly from those in 1 and 2 due to these conditional modifications. For example wild type azurin in 50 mM Ammonium Acetate pH 5.1 has a $S(\pi \rightarrow Cu(d_{x^2-y^2})$ LMCT band at 625 nm rather than 619 nm in 100 mM HEPES buffer at pH 8 as listed in Table 3.[25]

Table 3: UV- visible absorption properties reported in the literature are compared between wild type azurin, native nitrite reductase and the azurin Met121Gln variant

T1 Cu(II)	$S(\sigma) \rightarrow Cu(d_{x^2-y^2})$ **λ nm**	**ε $M^{-1}cm^{-1}$**	$S(\pi) \rightarrow Cu(d_{x^2-y^2})$ **λ nm**	**ε $M^{-1}cm^{-1}$**	**Buffer**	**pH**
WT-Azurin[25]	460	580	619	5100	100 mM HEPES	8
Native NiR[16]		-	595	-	20 mM MES	6
Azurin Met121Gln[25]	452	1200	610	6000	100 mM HEPES	8

Table 4: EPR properties reported in the literature are compared between wild type azurin, native nitrite reductase and the azurin Met121Gln variant

T1 Cu(II) EPR	A_z	A_x	A_y	g_z	g_x	g_y	**Buffer**	**pH**
WT-Azurin[25]	62	62	62	2.258	2.034	2.05	20 mM MOPS	7
Native NiR[16]	63	-	-	2.24	2.05	2.05	20 mM MES	6
Azurin Met121Gln[25]	57	29	35	2.287	2.025	2.077	20 mM MOPS	7

The third second generation variant (Phe15Trp) aims to address the kinetic component of the electron transfer rate by creating a more efficient physical pathway for the electron to travel from the T1 site to the T2 site. Tryptophan is known to assist in long

range electron transfer in biological systems. One example is in DNA photolyase; a solvent exposed tryptophan accepts an electron from the excited state of a flavin radical and transfers the electron to a nearby tryptophan.[26] The second tryptophan transfers the electron to a third tryptophan which ultimately reduces FADH to its catalytically active form.[26] These three tryptophans act as a wire to facilitate the electron transfer 15 Å in 30 ps.[26] Another example is in azurin, where an oxidant ($Re(I)(CO)_3(dmp)$) was linked to His124 on the surface of azurin and a tryptophan was placed between the oxidant and copper which were 19.4 Å apart.[27] It was shown that the rate of electron transfer had a low dependence on the driving force (potential difference between the redox pair) with the tryptophan model.[27] These examples demonstrate how tryptophan addresses the kinetic component of electron transfer. In native NiR, the T1 and T2 copper sites are covalently linked through the backbone of Cys136 which coordinates the T1 copper and His135 which coordinates the T2 copper (refer to Figure 6a).[28] The accepted theory is that the electron likely travels through this covalent linkage in native NiR.[28] In the first generation variant Az→NiR3His, the two copper sites are separated by approximately 11 Å with no obviously favorable pathway (refer to Figure 6b). The Phe15 residue which is mutated to Trp for this second generation variant is covalently linked to the T2 copper coordinating ligand His14. It is hypothesized that the electron will transfer from the T1 copper to Trp15 (an estimated 5.5 Å distance as shown in Figure 9) and be directed through the covalent linkage between Trp15 and His14 to the T2 copper.

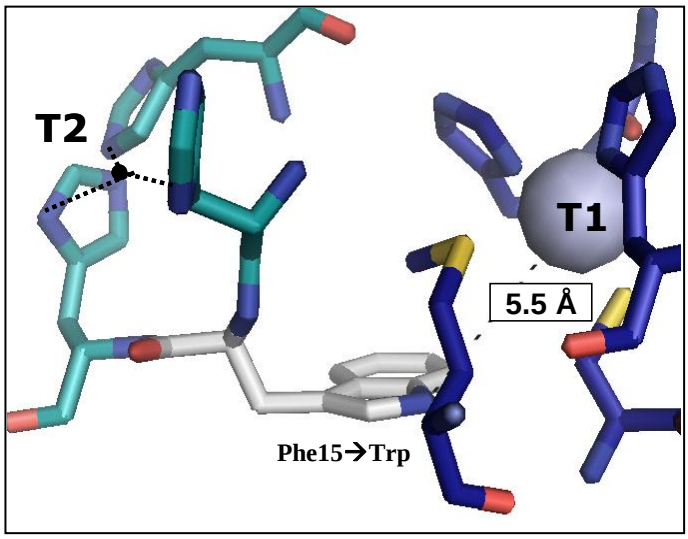

Figure 9: Pymol predicted structure for Az→NiR3His→Phe15Trp

These three mutations were layered onto the Az→NiR3His first generation model and characterized with UV-visible absorption spectroscopy, EPR spectroscopy, and cyclic voltammetry. The activity was measured with a Griess activity assay. These second generation mutations were also layered onto wild type azurin, Az→NiR, and two other first generation models. These other two first generation models are the focus of Chapter 2. They also use azurin as a protein scaffold to model the non-coupled dinuclear copper sites of the mammalian enzyme (Peptidyl glycine α-hydroxylating monooxygenase (PHM)) rather than nitrite reductase and therefore were named Az→PHM and Az→PHM3His.

1.2 Methods

1.2.1 Synthesis of Azurin Variants

The second generation mutations were layered onto existing first generation variants previously expressed and characterized in the Berry lab group.[9] The Yi Lu research group at the University of Illinois provided the gene for *Pseudomonas aeruginosa* azurin in a pET9a expression vector.[29] This vector includes a kanamycin resistance gene and allows for the control of azurin expression through a T7 promoter. The T7 RNA polymerase expression is induced by IPTG. The four, 1st generation variants (Az→PHM, Az→PHM3His, Az→NiR, and Az→NiR3His) were previously synthesized, expressed in *E. coli*, and characterized.[9]

The second generation mutations were layered onto the existing first generation variants (Az→PHM, Az→PHM3His, Az→NiR, and Az→Nir3His) and wild type azurin (WT) using the Stratagene Quikchange site-directed mutagenesis method. The homology of these first generation sequences in the primer annealing region for the Phe114Pro and Met121Gln made it possible to create one primer per mutation for all five existing sequences. The desired point mutation for Met121Glu created a restriction cut site for SmaI while for Phe114Pro the mutation deleted a cut site for PstI. Unfortunately, the sequences of the azurin variants were not all homologous in the primer annealing region for the Phe15Trp mutation, so three primers were designed, and the forward primers are shown in Figure 10. For each primer, a restriction enzyme cut site was either created or destroyed. Acaclone provided pDraw32 1.1.107 freeware software which was used to search for restriction sites within the primer annealing region. For Phe15Trp a SalI

restriction cut site was removed by incorporating a thymine rather than a cytosine base resulting in a silent point mutation highlighted in purple and with a box in Figure 10. This silent point mutation changes this codon for Val from GTC to GTT which according to the Kazusa codon usage database's *Escherichia coli* code, is more commonly used as a codon for Val in *E. coli*. This indicates protein translation will not be slowed down as a result of the silent point mutation.

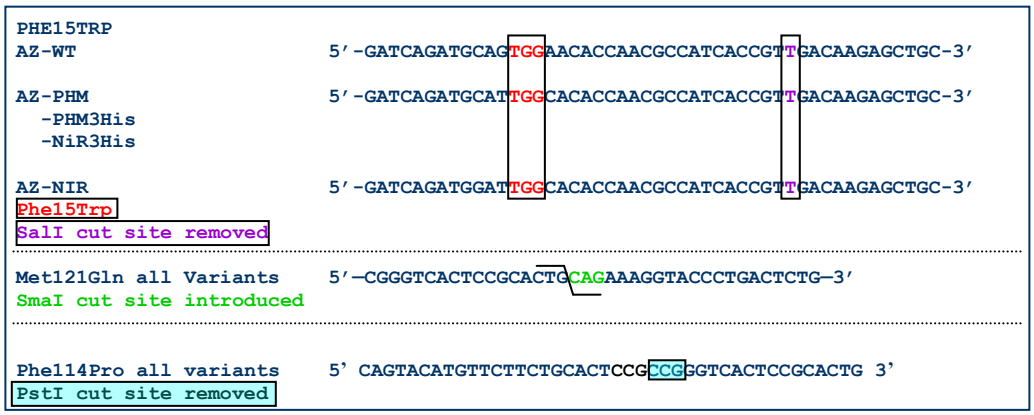

Figure 10: Primers were designed with the appropriate point mutation, as well as a restriction cut site modification for analysis.

The five primers listed above were purchased through Eurofins MWG Operon and diluted to 12.5 ng/μL in the thermocycler reaction mixture. Primstar Taq polymerase was used to amplify the DNA which incorporated the mutations from the primer into the copied DNA. The template DNA was methylated because it was purified from XL1-Blue *E. coli* cells; however the copied DNA was not methylated. Dpn1 took advantage of this key difference and was thus used to degrade the methylated template DNA, leaving a pure sample of the mutated copied DNA. The amplified linear DNA product was

confirmed with a 0.5% agarose gel which was run for 50 minutes at 95 volts and visualized with ethidium bromide (see Figure 11 and its legend)

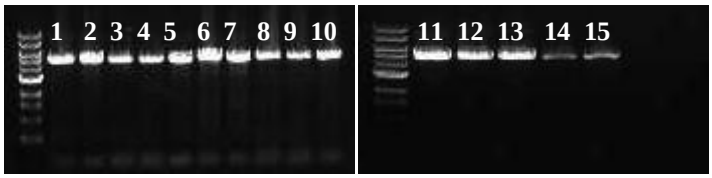

Figure 11: Thermocycler product visualization with 0.5% agarose gel. The amplified mutated DNA was confirmed with the single 4,752 base pair band. The content of each lane is provided in the legend below

Lane	Azurin Variant
1	WT→Phe114Pro
2	PHM→Phe114Pro
3	PHM3His→Phe114Pro
4	NiR→Phe114Pro
5	NiR3His→Phe114Pro
6	WT→Met121Gln
7	PHM→Met121Gln
8	PHM3His→Met121Gln
9	NiR→Met121Gln
10	NiR3His→Met121Gln
11	WT→Phe15Trp
12	PHM→Phe15Trp
13	PHM3His→Phe15Trp
14	NiR→Phe15Trp
15	NiR3His→Phe15Trp

Transformation of all 15 mutated DNA samples (the 3 individual mutations on 5 existing variants) were completed in freshly prepared competent XL1-Blue *E. coli* cells where the DNA was further amplified and purified using Wizard® *Plus* SV Minipreps DNA Purification System from Promega. Restriction digests were completed to confirm the presence of the mutation in the mini-prep DNA purified from overgrown XL1-Blue

E. coli cells. An example of the restriction analysis for the Phe114Pro variants is discussed in detail; however similar methods were used for the all of the five Met121Gln and the five Phe15Trp variants with unique restriction enzymes. SmaI restriction digest for Phe114Pro variants was completed at 25° C for 6 hours. SmaI cuts DNA that has the Phe114Pro mutation once, however without the mutation it cuts twice. Uncut plasmid DNA is a 4,752bp circular, supercoiled DNA so it travels faster than linear DNA across the 0.5% agarose gel (Figure 12). This gel was run for 2 hours at 100 volts. The digest shown in Figure 12 was completed on Az→PHM variants, however identical digests and results were observed for all five Phe114Pro variants (WT→Phe114Pro, Az→PHM→Phe114Pro, Az→PHM3His→Phe114Pro, Az→NiR→Phe114Pro, Az→Nir3His→Phe114Pro). Similarly, this was repeated with unique restriction enzymes for the Met121Gln and Phe15Trp variants. The results were used to determine mini-prep DNA sample, should be used to complete midi-prep DNA purification. In this example, the mini-prep DNA from colony # 2 – 2 (Figure 12, lane 5) was chosen.

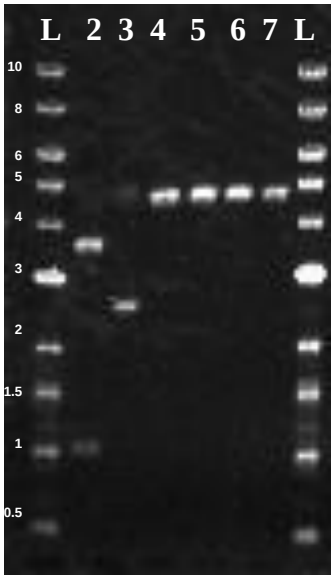

Figure 12:
0.5 % agarose gel analysis of Az→PHMPhe114Pro restriction digest with SmaI and its legend shown right

Lane	Azurin variant and expected fragment sizes
2	Az→PHM-cut with SmaI (expected 3700bp, 1100 bp)
3	Az→PHM-uncut (expected 4752bp circular)
4	Mini-prep DNA from XL1-Blue *E. Coli* transformed colony # 2-1 Az→PHM Phe114Pro - cut with SmaI (expected 4752bp linear)
5	Mini-prep DNA from XL1-Blue *E. Coli* transformed colony # 2-2 Az→PHM Phe114Pro - cut with SmaI (expected 4752bp linear)
6	Mini-prep DNA from XL1-Blue *E. Coli* transformed colony # 2-3 Az→PHM Phe114Pro - cut with SmaI (expected 4752bp linear)
7	Mini-prep DNA from XL1-Blue *E. Coli* transformed colony # 2-4 Az→PHM Phe114Pro - cut with SmaI (expected 4752bp linear)

The restriction digest was repeated after competent XL1-Blue *E. coli* were transformed with mini-prep DNA from colony # 2 – 2 and purified with a Wizard® *Plus* SV Midipreps DNA Purification System from Promega. This second digest confirmed the presence of the mutation in the midi-prep DNA. This gel (Figure 13) was also run for 2 hours at 100 volts. The results shown are for the WT→Phe114Pro and Az→PHM→Phe114Pro variants; however identical methods and results were observed for all five Phe114Pro variants (WT→Phe114Pro, Az→PHM→Phe114Pro, Az→PHM3His→Phe114Pro, Az→NiR→Phe114Pro, and Az→Nir3His→Phe114Pro).

Again restriction digestion confirmed the incorporation of the primer into the azurin gene within the pET9a expression vector.

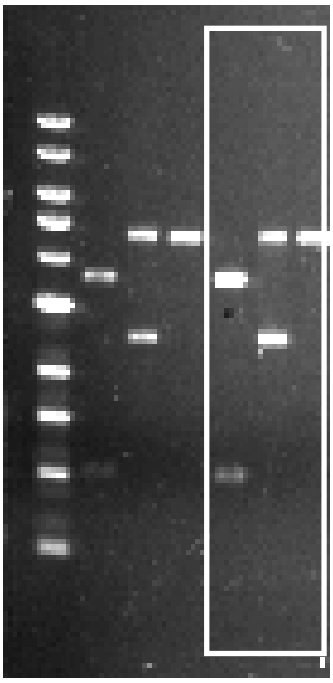

Lane	Azurin variant and expected fragment sizes
2	WT-cut with SmaI (expected 3700bp, 1100 bp)
3	WT-uncut (expected 4752bp circular)
4	Midi-prep DNA from XL1-Blue *E. Coli* transformed colony # 1-1 WT Phe114Pro - cut with SmaI (expected 4752bp linear)
5	Az→PHM-cut with SmaI (expected 3700bp, 1100 bp)
6	Az→PHM-uncut (expected 4752bp circular)
7	Midi-prep DNA from XL1-Blue *E. Coli* transformed colony # 2-2 Az→PHM Phe114Pro - cut with SmaI (expected 4752bp linear)

Figure 13: 0.5% Agarose gel restriction digest analysis of Midi-Prep DNA confirmed the presence of the Phe114Pro mutation

DNA sequencing results are shown on the following two pages for the Az→PHM→Phe114Pro variant which were obtained from the University of Minnesota Biomedical Genomics Center. Just as restriction digest analysis was completed for all 15 variants, the DNA was also sequenced for all 15 to confirm the presence of each mutation. The sequenced DNA (named "Exp" in the following alignment) was aligned with the theoretical DNA (named "Theore") for each variant. The complete azurin gene and several nucleotides following the gene where 100% homology was observed, is highlighted in yellow and the primer and Phe114Pro mutation are distinguished.

```
Comparison of:
(A)     Theoretical     PHM Phe114Pro 4752 bp
(B)     Experimental    PHM Phe114Pro 1272 bp

99.5% identity in 1012 nucleotide overlap


             3810      3820      3830      3840      3850      3860
Theore AGCTGGCTGCAGTGTCTCTGCTGTCTCTGCTGTCTGCTCCGCTGCTGGCTGCTGAATGCT
       ::::::::::::::::::::::::::::::::::::::::::::::::::::::::::::
Exp    AGCTGGCTGCAGTGTCTCTGCTGTCTCTGCTGTCTGCTCCGCTGCTGGCTGCTGAATGCT
             70        80        90       100       110       120

             3870      3880      3890      3900      3910      3920
Theore CCGTTGATATCATGGGTAATGATCAGATGCATTTCCACACCAACGCCATCACCGTCGACA
       ::::::::::::::::::::::::::::::::::::::::::::::::::::::::::::
Exp    CCGTTGATATCATGGGTAATGATCAGATGCATTTCCACACCAACGCCATCACCGTCGACA
            130       140       150       160       170       180

             3930      3940      3950      3960      3970      3980
Theore AGAGCTGCAAGCAGTTCACTGTTAACCTGTCTCACCCAGGTAACCTGCCGAAGAACGTTA
       ::::::::::::::::::::::::::::::::::::::::::::::::::::::::::::
Exp    AGAGCTGCAAGCAGTTCACTGTTAACCTGTCTCACCCAGGTAACCTGCCGAAGAACGTTA
            190       200       210       220       230       240

             3990      4000      4010      4020      4030      4040
Theore TGGGTCACAACTGGGTTCTGTCCACCGCGGCTGACATGCAAGGCGTTGTCACTGACGGTA
       ::::::::::::::::::::::::::::::::::::::::::::::::::::::::::::
Exp    TGGGTCACAACTGGGTTCTGTCCACCGCGGCTGACATGCAAGGCGTTGTCACTGACGGTA
            250       260       270       280       290       300

             4050      4060      4070      4080      4090      4100
Theore TGGCTAGCGGTCTGGATAAAGACTACCTGAAGCCGGATGACTCTCGAGTTATCGCCCACA
       ::::::::::::::::::::::::::::::::::::::::::::::::::::::::::::
Exp    TGGCTAGCGGTCTGGATAAAGACTACCTGAAGCCGGATGACTCTCGAGTTATCGCCCACA
            310       320       330       340       350       360

             4110      4120      4130      4140      4150      4160
Theore CCAAGCTGATCGGATCCGGTGAAAAAGACTCCGTTACTTTCGACGTTTCCAAGCTTAAAG
       ::::::::::::::::::::::::::::::::::::::::::::::::::::::::::::
Exp    CCAAGCTGATCGGATCCGGTGAAAAAGACTCCGTTACTTTCGACGTTTCCAAGCTTAAAG
            370       380       390       400       410       420

             4170      4180      4190      4200      4210      4220
Theore AAGGTGAACAGTACATGTTCTTCTGCACTCCGCCGGGTCACTCCGCACTGATGAAAGGTA
       ::::::::::::::::::::::::::::::::::::::::::::::::::::::::::::
Exp    AAGGTGAACAGTACATGTTCTTCTGCACTCCGCCGGGTCACTCCGCACTGATGAAAGGTA
            430       440       450       460       470       480

             4230      4240      4250      4260      4270      4280
Theore CCCTGACTCTGAAATAGAGATCCGGCTGCTAACAAAGCCCGAAAGGAAGCTGAGTTGGCT
       ::::::::::::::::::::::::::::::::::::::::::::::::::::::::::::
Exp    CCCTGACTCTGAAATAGAGATCCGGCTGCTAACAAAGCCCGAAAGGAAGCTGAGTTGGCT
            490       500       510       520       530       540
```

```
             4290       4300       4310       4320       4330       4340
Theore GCTGCCACCGCTGAGCAATAACTAGCATAACCCCTTGGGGCCTCTAAACGGGTCTTGAGG
       ::::::::::::::::::::::::::::::::::::::::::::::::::::::::::::::
Exp    GCTGCCACCGCTGAGCAATAACTAGCATAACCCCTTGGGGCCTCTAAACGGGTCTTGAGG
            550        560        570        580        590        600

             4350       4360       4370       4380       4390       4400
Theore GGTTTTTTGCTGAAAGGAGGAACTATATCCGGATATCCACAGGACGGGTGTGGTCGCCAT
       ::::::::::::::::::::::::::::::::::::::::::::::::::::::::::::::
Exp    GGTTTTTTGCTGAAAGGAGGAACTATATCCGGATATCCACAGGACGGGTGTGGTCGCCAT
            610        620        630        640        650        660

             4410       4420       4430       4440       4450       4460
Theore GATCGCGTAGTCGATAGTGGCTCCAAGTAGCGAAGCGAGCAGGACTGGGCGGCGGCCAAA
       ::::::::::::::::::::::::::::::::::::::::::::::::::::::::::::::
Exp    GATCGCGTAGTCGATAGTGGCTCCAAGTAGCGAAGCGAGCAGGACTGGGCGGCGGCCAAA
            670        680        690        700        710        720

             4470       4480       4490       4500       4510       4520
Theore GCGGTCGGACAGTGCTCCGAGAACGGGTGCGCATAGAAATTGCATCAACGCATATAGCGC
       ::::::::::::::::::::::::::::::::::::::::::::::::::::::::::::::
Exp    GCGGTCGGACAGTGCTCCGAGAACGGGTGCGCATAGAAATTGCATCAACGCATATAGCGC
            730        740        750        760        770        780

             4530       4540       4550       4560       4570       4580
Theore TAGCAGCACGCCATAGTGACTGGCGATGCTGTCGGAATGGACGATATCCCGCAAGAGGCC
       ::::::::::::::::::::::::::::::::::::::::::::::::::::::::::::::
Exp    TAGCAGCACGCCATAGTGACTGGCGATGCTGTCGGAATGGACGATATCCCGCAAGAGGCC
            790        800        810        820        830        840

             4590       4600       4610       4620       4630       4640
Theore CGGCAGTACCGGCATAACCAAGCCTATGCCTACAGCATCCAGGGTGACGGTGCCGAGGAT
       ::::::::::::::::::::::::::::::::::::::::::::::::::::::::::::::
Exp    CGGCAGTACCGGCATAACCAAGCCTATGCCTACAGCATCCAGGGTGACGGTGCCGAGGAT
            850        860        870        880        890        900

             4650       4660       4670       4680       4690       4700
Theore GACGATGAGCGCATTGTTAGATTTCATACACGGTGCCTGACTGCGTTAGCAATTTAACTG
       ::::::::::::::::::::::::::::::::::::::::::::::::::::::::::::::
Exp    GACGATGAGCGCATTGTTAGATTTCATACACGGTGCCTGACTGCGTTAGCAATTTAACTG
            910        920        930        940        950        960

             4710       4720       4730       4740       4750
Theore TGATAAACTACCGCATTAAAGCTTATCGATGATAAGCTGTCAAACATGAGAA
       :::::::::::::::::::::::::::::::::::::::::::::::::::
Exp    TGATAAACTACCGCATTAAAGCTTATCGATGATAAGCTGTCAAACATGAGAA
            970        980        990       1000       1010
```

Figure 14: DNA sequence alignment for sequenced midi-prep Az→PHM Phe114Pro DNA with the theoretical DNA for Az→PHM Phe114Pro. The primer is not highlighted in yellow, however the Phe114Pro mutation has been highlighted in teal.

The sequenced midi-prep DNA was transformed into competent BL21* *(DE3) E. coli* for protein expression as is outlined in previous publication.[9] Protein was expressed in yields ranging from 20 – 100 mg/L for six of the fifteen total second generation variants (the three wild type azurin variants and the three Az→NiR3His variants). The focus of the characterization and activity of these second generation variants is for wild type azurin and the Az→NiR3His second generation variants because Az→NiR3His had the most activity of the first generation variants. The wild type azurin variants were done as a control and for comparison.

1.2.2 Sample Preparation

Copper was bound to the T1 site with ¼ equivalent titrations of $CuSO_4$ into the protein sample in 50 mM NH_4OAc, pH 6.35 while stirring at 4° C until the peak of the LMCT band near 625 nm reached a maximum. Samples containing Hg^{+2} in the T1 site were prepared for Az→NiR3His variants after determining the concentration of copper required to saturate the type one site. The same concentration of $HgCl_2$ was used to saturate the T1 site with mercury. Buffer exchange to 50 mM NH_4OAc pH 5.1 and removal of excess copper or mercury was accomplished with disposable PD-10 desalting columns packed with Sephadex™ G-25 medium. The protein was concentrated to the desired concentration for each given method with Amicon Centricon centrifugal filter devises with a membrane pore size of 10 kDa. For cyclic voltammetry approximately 100 μM concentrations were desired while 2 mM concentrations were used for EPR samples. Copper was bound to the T2 site by titrating 0.75 more equivalents of copper for the EPR samples. The 2 mM EPR sample was diluted to 1 mM with glycerol and 10 μL of this sample were removed and diluted 1:10 in 50 mM NH_4OAc pH 5.1 for UV-visible absorption spectroscopy. The remaining 1 mM EPR sample was flash frozen in glass EPR tubes and stored at 77 K in liquid nitrogen.

1.2.3 EPR and Absorptivity Measurements

The absorbance of each EPR sample was measured at 20 °C with a Shimadzu UV2401 PC UV-visible recording spectrophotometer. EPR was performed with an X-band Varian V7200 electromagnetic assembly interfaced with an oscilloscope and analog to digital signal converter. The average of two scans was taken for each spectrum and ten spectra were averaged for each sample. Each scan was collected at a frequency of 9.027 GHz, 0.5 mW power, in liquid nitrogen (77 K), and the modulation amplitude was 5 G. The EPR spectra were integrated with the SIMPOW6 program.[30]

The absorptivity value of for each variant was determined by the relationship between Beer's law ($A = \varepsilon lc$), concentration and the area under the EPR signal as shown in Equation 1.

$$\iint EPR = \alpha * c = \alpha * (A / \varepsilon l) \qquad \text{Equation [1]}$$

Where $\iint EPR$ = Area under the EPR spectra is proportional to concentration (c)

A = absorbance of LMCT band near 625 nm

l = path length = 1 cm

ε = molar absorptivity coefficient ($M^{-1}cm^{-1}$)

α = proportionality constant

The proportionality constant α was solved for using the known molar absorptivity coefficient of wild type azurin (5000 $M^{-1}cm^{-1}$) and the measured absorbance and area under the EPR spectrum.[31, 32] This proportionality constant along with UV-visible measurements and the area under the EPR signal for each variant were used with this relationship to solve for the molar absorptivity of each variant.

1.2.4 Cyclic Voltammetry

Cyclic voltammetry scans were conducted in CH instruments Picoamp booster and Faraday cage at 20 °C under argon gas with CH instruments CHI620B potentiometer with a pyrolytic graphite edge (PGE) working electrode (polished for 1 – 5 minutes with 0.05 micron alumina powder). A platinum wire counter electrode and a Ag / AgCl reference electrode (212 mV standard) were used for each scan. Typical scanning parameters were a 50 mV/s scan rate, 1×10^{-7} sensitivity and a 1 second quiet time between scans. The potential of the cathodic and anodic peaks were determined by drawing a baseline using CH instrument 620B electrochemical analyzer software and allowing the software to find the peak with the given baseline correction.

1.2.5 Griess Activity Assay

The Griess assay had previously been completed for the first generation Az→NiR3His variant. Upon characterizing the second generation models, I began optimizing the assay conditions using the second generation variant Az→NiR3His→MET121GLN as the catalyst for the reaction. A 250 μM Az→NiR3His→Met121Gln sample bound with 1.75 equivalents of copper was stirred under argon gas in 50 mM ammonium acetate pH 5.5 with 1 mM sodium nitrite as the substrate. Ascorbic acid was used as a reductant and was in a 78 fold excess to copper. The zero time assay point was collected prior to adding ascorbate to the reaction. Each assay point was collected by first diluting a small aliquot of the previously discussed reaction 25 fold with 50 mM ammonium acetate pH 5.1 in 500 μL total volume. This 500 μL sample was thoroughly mixed first with 500 μL 1% sulfanilamide in 3M HCl, followed by 500 μL 0.02% napthyl ethylene diamine (NED) in water and left to react at 20° C for 10 minutes.[33] The absorbance at 540 nm was measured and plotted versus time.

1.3 Results and Discussion

1.3.1 Characterization of the 2nd Generation Models with UV-Vis

The UV-visible absorption measurements of for the second generation mutations layered onto wild type (WT) azurin and Az→NiR3His are shown in Figure 15. An intense $S_{Cys}(\pi) \rightarrow Cu(d_{x^2-y^2})$ LMCT is observed for wild type azurin and the Phe15Trp variants at 625 nm; however for the Met121Gln and Phe114Pro variants, 615 nm and 600 nm wavelengths, respectively, are observed (shown in Table 7). These transitions are the result of energy in the form of ultraviolet light exciting an electron from the p orbital (highest occupied sulfur molecular orbital (HOMO)) of the sulfur atom from Cys112, to the Cu $d_{x^2-y^2}$ orbital (singly occupied copper molecular orbital (SOMO)). The intensity (molar absorptivity coefficient) of the charge transfer is proportional to the overlap of HOMO and SOMO.

Table 5: Molar absorptivity coefficients for the second generation variants as were calculated from Equation 1 and correspond (each uniquely represented by color) to the spectra shown in Figure 15.

Azurin Variant	λ (nm)	ε ($M^{-1}cm^{-1}$)
WT	625	5000
WTPhe114Pro	600	4400
WTMet121Gln	615	5600
WTPhe15Trp	625	5700
NiR3HisPhe114Pro	600	4000
NiR3HisMet121Gln	615	3700
NiR3HisPhe15Trp	625	3700

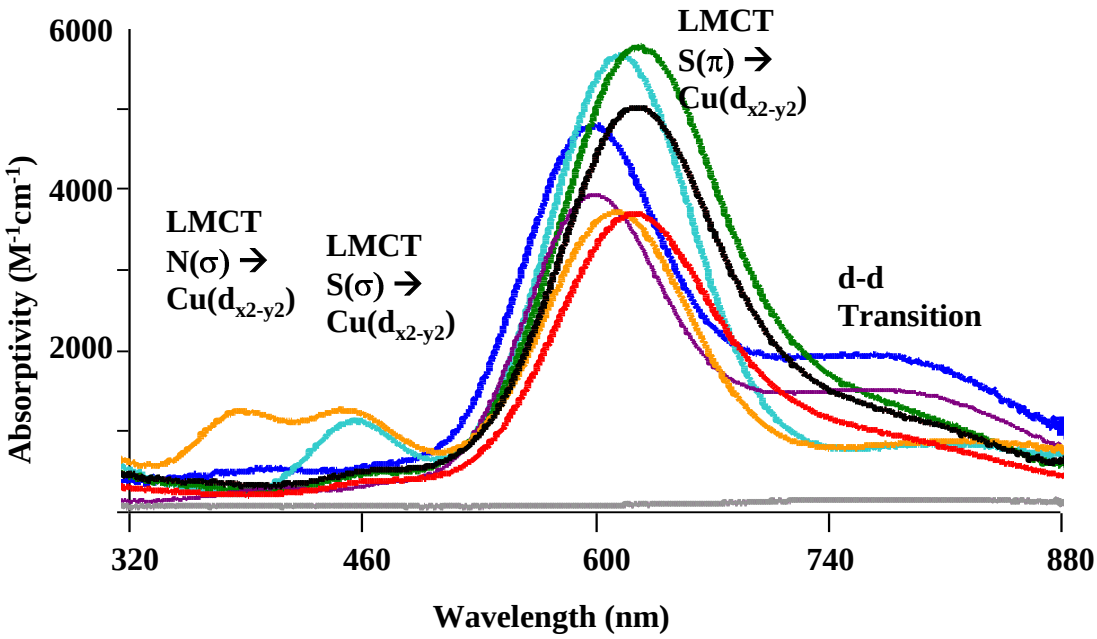

Figure 15: UV-Visible absorption for all second generation models is overlaid with wild type azurin. The colors correspond to those shown in Table 5.

a) WT–Azurin and Phe15Trp Sπ→Cu LMCT at 625 nm

Typical blue copper proteins which have a distorted tetrahedral geometry, have a $S_{Cys}(\pi) \rightarrow Cu(d_{x^2-y^2})$ LMCT at 600 nm, which is higher in energy than the 625 nm band observed in wild type azurin. The energy of LMCT bands increase as the field strength of the ligands increase.[34] These energies are also dependent on the distortion of the axial and equatorial bonds.[34] In wild type azurin, the axial ligands are positioned on the z-axis and are further away from copper than in typical blue copper proteins. As a result, it would be expected for the Cu $d_{x^2-y^2}$ orbital to increase in energy, and the Cu d_{z^2} orbital should decrease in energy due to a weaker ligand field on the z-axis; however this is not observed. Wild type azurin has a lower energy charge transfer band than typical T1 Cu

proteins even though azurin has distorted trigonal bypyramidal geometry with two weaker axial ligands (Met, backbone carbonyl) and three planar ligands (His_2Cys). If only the axial ligands were considered, the Cu $d_{x^2-y^2}$ orbital would be expected to have a higher energy level and thus a higher energy LMCT; however this is not the case. Increased covalency of the $S_{Cys}\pi$–Cu($d_{x^2-y^2}$) bond as a result of having weaker axial ligands in azurin, decreases the energy level of the Cu $d_{x^2-y^2}$ orbital because the Cu $d_{x^2-y^2}$ orbital has some Sπ orbital character which is lower in energy. Additionally, the energy level of the Sπ orbital is increased as a result of this covalency, because it has more Cu $d_{x^2-y^2}$ orbital (higher energy) character. Thus, the difference in energy between Sπ and Cu $d_{x^2-y^2}$ is smaller, meaning that it would require less energy to excite an electron from the $S_{Cys}\pi$ orbital to the Cu $d_{x^2-y^2}$.

Similar to azurin, the Phe15Trp variants maintain the LMCT at 625 nm indicating the T1 site still binds copper after introducing a tryptophan between the two copper sites. The strong LMCT band at 625 nm was the first evidence collected to indicate that the tryptophan mutation did not disrupt azurin protein folding or interfere with the T1 copper geometry.

b) Phe114Pro variants Sπ→Cu LMCT at 600 nm

The higher energy transitions at 600 nm observed for the Phe114Pro variants are closer to those of blue copper proteins with distorted tetrahedral geometry. It is thought that the Phe114Pro mutation decreases the covalency of the S – Cu bond. The crystal structure for this variant indicated that copper moved up out of the plane created by the three equatorial ligands (His_2Cys), which would result in a more tetrahedral geometry.

The higher energy LMCT is a result of the overall increased ligand field strength for the Phe114Pro variant and the decreased covalency of the Cu – S bond.

c) Met121Gln variants S→Cu LMCT at 615 nm and 460 nm

In the Met121Gln variant, the higher energy of this $S_{Cys}(\pi) \rightarrow Cu(d_{x^2-y^2})$ charge transfer is also due to the geometric distortions. The ligand field strength increases as a result of replacing the axial S_{Met} with O_{Gln}, because the oxygen atom from Gln is a better ligand for copper. The ligand - ligand repulsions and orbital overlap differences are likely the cause of this shift.[34] The geometric distortions resulting from the Met121Gln mutation also gave rise to a LMCT at 460 nm. This has been assigned as $S_{Cys}(\sigma) \rightarrow Cu(d_{x^2-y^2})$ LMCT and is a result of the S – Cu bond having more σ character than π character. The increased intensity of the LMCT band at 460 nm is further indication that the orbital overlap has changed.

d) Molar Absorptivity Coefficients

The Phe114Pro variants are in range with the literature reported charge transfer which is 599 nm with a molar absorptivity coefficient of 4300 M^{-1} cm^{-1}.[24] The Met121Gln variants are also similar to the literature reported charge transfer which is 610 nm with a molar absorptivity coefficient of 6000 M^{-1} cm^{-1}, however the experimental wavelength was 5 nm less than the literature.[25] The 5 nm difference between the literature and experimental wavelengths was also observed for wild type azurin; however the literature reported values were obtained in a different buffer at a higher pH which may result in this shift.[25]

The molar absorptivity coefficient for the $S_{Cys}(\pi) \rightarrow Cu(d_{x^2-y^2})$ LMCT was calculated for each variant and is listed in Table 5. The WT-variants have molar absorptivity coefficients approximately 1000 $M^{-1}cm^{-1}$ greater than those for the NiR3His - variants. The method for determining these coefficients (discussed in section **1.2.3** of this thesis) is most accurate for copper proteins; however it is still prone to error. The concentrations of protein in these samples may vary slightly due to the approximate method used to concentrate the protein and to measure and add glycerol to the EPR sample. The four wild type absorptivity calculations were completed at the same time with the exact same instrument gain for the EPR signal, as opposed to the NiR3His variants which were slightly less concentrated. The gain of the EPR signal was increased for the NiR3His variants to obtain a better signal to noise ratio. Controls were run to determine how to correct for the gain of the instrument. It was determined that under identical frequency and time constants, the gain was a direct multiplied factor which was applied to each spectrum prior to determining the area under the peak. After all signals were shown to be under the same amplification factor (gain), the area under the signal was used to solve for the molar absorptivity coefficient. The NiR3His samples which were less concentrated would still have a smaller signal to noise ratio than that of the more concentrated samples. The additional noise increases the area under the EPR signal which in turn results in a value lower than the actual molar absorptivity coefficient. Repeating the experiment at a higher concentration would determine whether or not this was the source of deviation.

1.3.2 Characterization of the 2nd Generation Models with EPR

a) Second Generation Phe114Pro Characterization

The Phe114Pro variants exhibit similar EPR spectra to that of wild type azurin with a few small differences discussed here. The g_z-value represents the ground state splitting into the energy level associated with the + ½ and - ½ spin states when the magnetic field is parallel to the axial ligand direction, and it is also dependent on the energy of the d_{x2-y2} orbital.[34] The Phe114Pro mutation has a smaller g_z-value (shown in Table 5) than wild type azurin, which may result from a stronger ligand field. A stronger ligand field may result from the closer proximity of copper to S_{Met121}. The hypothesis that there is a stronger ligand field for the Phe114Pro variant than for wild type azurin is also supported by the higher energy LMCT band in the UV-visible absorption spectrum at 600 nm for Phe114Pro, because a stronger ligand field would increase the energy of this LMCT band.

There is less strain (broadening of the hyperfine structure) in the Phe114Pro EPR spectrum than in the wild type azurin spectrum (comparison is made between the top EPR spectrum in blue to that of the Phe114Pro spectrum shown just below it in red of Figure 16). Strain is commonly observed in copper protein EPR and is a result of the tertiary structure of the protein dictating non-ideal ligand coordination to copper. It is hypothesized that the strain in wild type azurin is the result of distortions which may be due to the rigidity of the secondary coordination sphere surrounding the T1 copper site. There is little conformational strain observed in the EPR spectra for the Phe114Pro variant which means the ligand interactions with copper are less constrained by the

secondary coordination sphere. This means that the mutation has not only interfered with the interaction between the backbone carbonyl of Gly45, but has also altered the secondary coordination sphere. Phe residues in the secondary coordination sphere have been linked to an increased reduction potential of the T1 copper site by as much as 30 mV.[35] Replacing phenylalanine with proline may contribute to the lower reduction potential for this mutation in addition to disrupting the Gly45 backbone carbonyl's coordination to copper.

One advantage to studying models where azurin is the scaffold is that we can selectively bind the T1 site with mercury. The coordinating S_{Cys} ligand in the T1 site is soft which preferentially binds to mercury, a much softer ligand than copper. Mercury(II) is EPR silent due to the d^{10} electron configuration. This allows us to examine only the EPR spectrum of the T2 copper site. The T2 copper spectrum (represented in yellow by the NiR3His→Phe114Pro T1Hg T2Cu spectra Figure 16) is equivalent to that of the first generation NiR3His variant, indicating the modeled T2 site has not been disrupted as a result of this mutation.

The addition of the individual T1 and T2 copper EPR spectra for the NiR3His variants is expected to overlay with the spectrum collected after populating both sites with copper (the bottom spectrum in purple of Figure 16 is NiR3His→Phe114Pro T1Cu T2Cu). This expected result was observed in Figure 16 and indicates that populating the T2 site does not result in any conformational changes to the T1 copper.

Table 6: Experimental EPR parameters for Phe114Pro variants are compared. The literature A_z for Phe114Pro is 54 G and the g_z – value is 2.209.[24]

Sample	A_z (G)	g_z
Free Cu	126	2.41
WT	62	2.24
WTPhe114Pro	66	2.20
NiR3His Phe114ProT1Cu	66	2.20
NiR3His Phe114Pro T1HgT2Cu	171	2.28

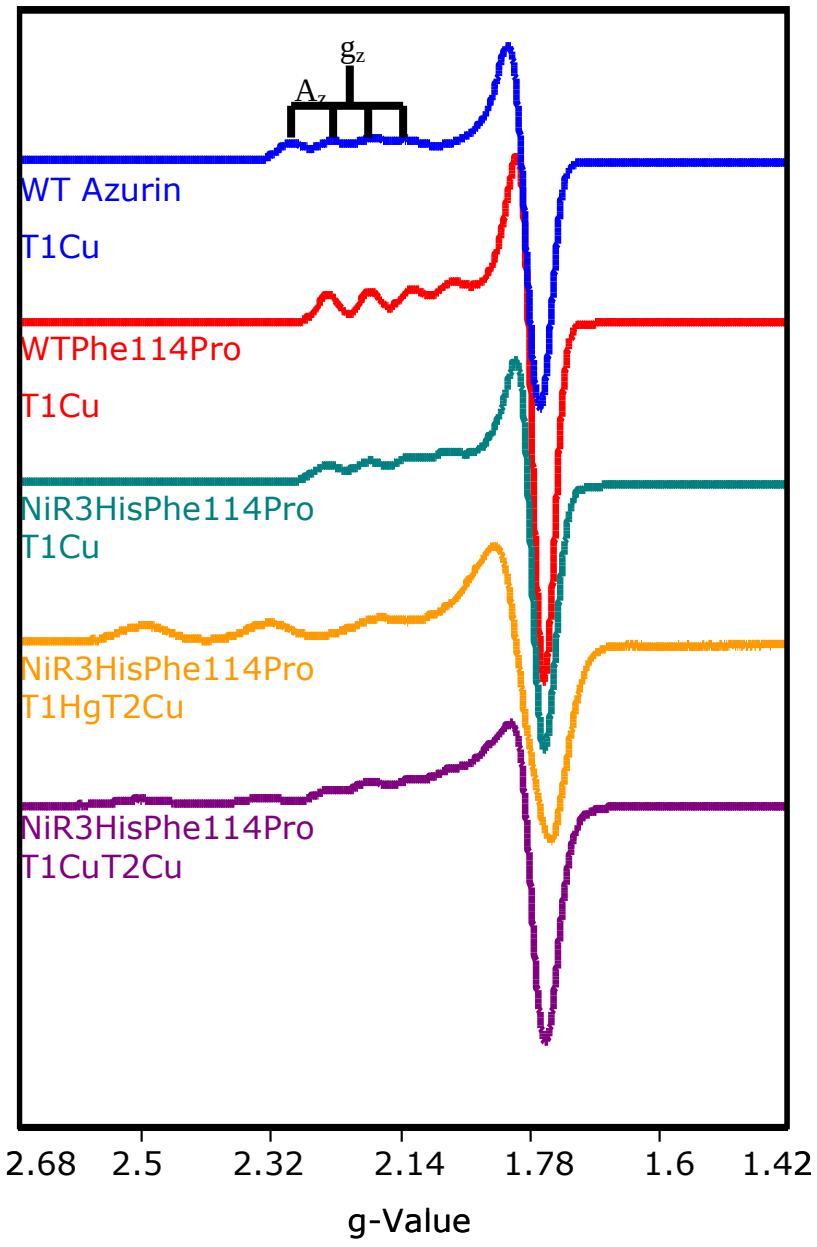

Figure 16: EPR spectra for the second generation Phe114Pro variants designed to reduce the potential of the type one copper site is compared to wild type azurin. The experimentally determined A_z and g_z – values were previously represented in Table 6.

b) Second Generation Met121Gln Characterization

Simulations for the WT-Met121Gln EPR signal shown in Figure 17 still need to be completed; however the A_z-values and g_z-values approximated from the spectra are listed in Table 7. The experimental WT→Met121Gln spectrum overlays well with simulated spectra for the previously synthesized and crystallized azurin Met121Gln mutant in the literature.[25] The literature reported values are shown in Table 4 in section **1.4.1** of this thesis. The g_z-value and A_z-value is in agreement with the literature, however the A_z-value is 2 Gauss larger in the literature. This is most likely a result of the different methods used to determine the A_z-value. The A_z and g_z values for the T2 copper site of native NiR and Az→NiR3His→Met121Gln are also listed in Table 7, The g_z-value is near the literature value for the T2 copper site, however the A_z-value is slightly larger for the model. Again, this may be due to the different methods used to determine the experimental A-value.[25] Additionally, the A_z-value for the T2 copper native NiR spectrum is more difficult to derive than in our model because the native NiR EPR spectrum is a mixture of the T1 and T2 sites. The A_z-value for the T2 site for our model however was determined without the T1 site bound to copper, making it easier to distinguish the signal. These values not only confirm that the T2 copper site is a good spectroscopic model for NiR, but also confirms that the T2 site has not been disrupted as a result of the mutation, and the modeled T2 site is spectroscopically similar to native NiR. The sum of the NiR3His T1 copper bound spectrum and the T2 copper bound spectrum yields the Az→NiR3His spectrum with both sites bound to copper. This indicates both sites in fact bind copper and are not spectroscopically coupled.

Table 7: EPR parameters for Met121Gln estimated from Figure 17

Sample	A_z (G)	g_z
Free Cu	**126**	**2.41**
WT	**62**	**2.24**
WT→Met121Gln	**55**	**2.29**
Az→NiR3His→ Met121Gln T1Cu	**37**	**2.28**
Az→NiR3His→ Met121Gln T1HgT2Cu	**177**	**2.27**

The hyperfines observed in the g_x and g_y region of the spectrum for the T1 site of the Met121Gln variants (Figure 17) are most likely a consequence of lowered symmetry. Previously crystallized structures of this variant suggest a conformational change from the trigonal bipyramidal geometry observed for wild type azurin.[36] There is axial symmetry in the wild type copper site because of the trigonal bipyramidal coordination. There is loss of symmetry when glutamine coordinates copper through its oxygen atom forming a much stronger bond with copper than S_{Met} does. The oxygen is closer to copper than the sulfur was and oxygen is also a better ligand for copper because they are both hard atoms. The strong interaction between copper and the axial glutamine causes copper to fall 0.26 Å deeper past the His_2Cys plane, closer to the axial Gly backbone carbonyl (refer back to Figure 8 for clarification).[36] The mutation also induces further protein conformational changes which create a stronger interaction between the His117 and copper in the reduced state. The distance between His117 and copper is 0.68 Å longer in the reduced state than in the oxidized state.[36] Copper in its reduced form lies closer to the plane defined by the trigonal coordinating residues Cys112, His46, and His117.[36] The

imidazole ring of His46 rotates 17° moving backwards 0.46 Å.[36] The oxygen on Gln121 shifts 0.52 Å in the opposite direction of the His46 when copper is reduced.[36] As a result the bond angle between Cys-S – Cu(I) – N-His46 is now nearly linear, causing S_{Cys112} and N_{His46} to be much stronger ligands than the rest.[36] This indicates that these large conformational changes resulting from the Met121Gln mutation, could result in greater flexibility surrounding the T1 copper site which may be responsible for the additional hyperfine observed in the parallel region of the NiR3His→Met121Gln $T1^{Cu}$ EPR spectrum. It may be possible for copper to bind the type one site in more than one conformation resulting in two possible geometries. The mutations on nearby residues 10, 14, and 16 which were completed for the first generation NiR3His variant may somehow stabilize this other geometry.

The alignment between the Cu d_{x2-y2} and His46-Nσ orbitals would change as a result of the conformational change discussed. This may explain the N(σ)→Cu(d_{x2-y2}) LMCT band at 360 nm in the UV-visible absorption spectrum for NiR3His→Met121Gln, however this theory would be better supported if copper were reduced. The copper must remain in the oxidized form for both confirmations according to both the EPR and the UV-visible spectra because the reduced form of copper has a d^{10} electron configuration. This means that all electrons are paired, so no splitting in the EPR signal would be observed nor would any LMCT bands be observed in the UV-visible spectrum because the Cud_{x2-y2} orbital is already filled.[37]

The sigma character of the Cu - S_{Cys} bond is similarly strong in the green copper NiR isoform. Strong LMCT bands at 360 nm, 460 nm and 570 nm are also observed for

green copper NiR, however the peak at 360 nm has been assigned as a weak S_{Met} – Cu charge transfer.[38] This cannot be the case for the Az→NiR3His→Met121Gln variant because there is no axial methionine.[38] This second generation variant may be a better spectroscopic model of the green copper NiR than for the blue.

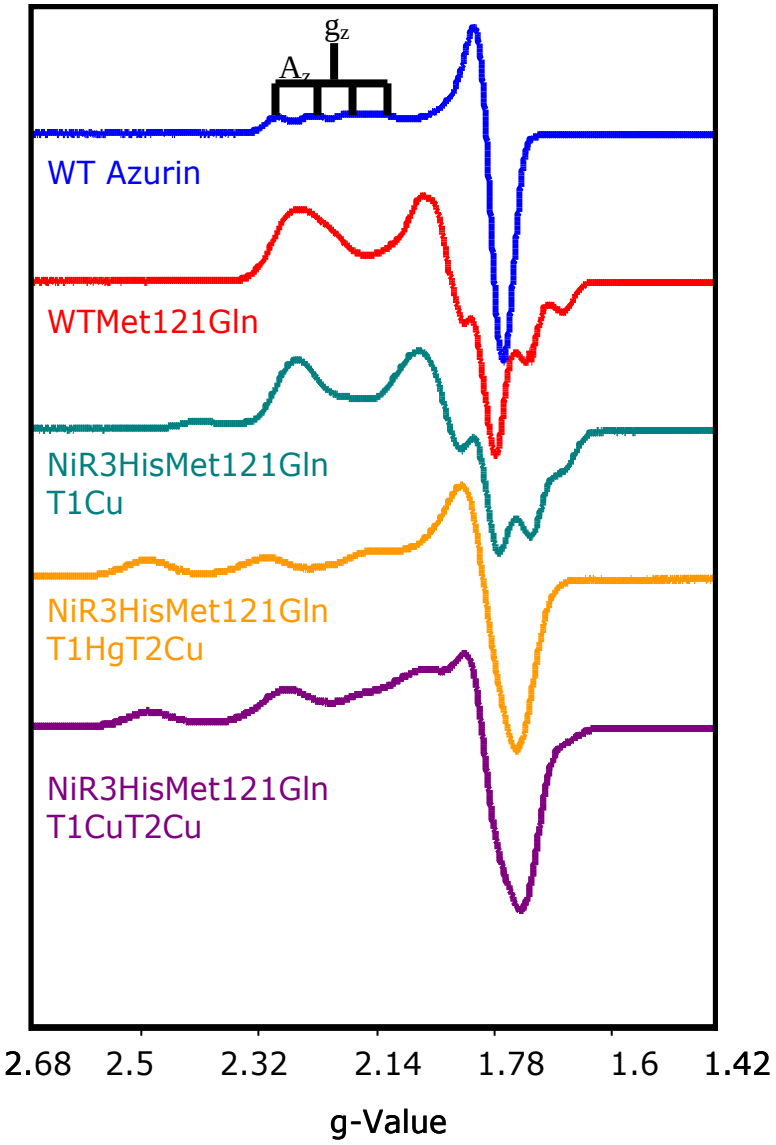

Figure 17: EPR Spectra for the second generation variant Met121Glu designed to lower the reduction potential of the T1 copper site. The corresponding parameters were previously shown in Table 7.

c) Second Generation Phe15Trp Characterization

The EPR spectra for the Phe15Trp variants were expected to be identical to those of the first generation models because the mutation was incorporated between the two copper sites and should therefore have no effect on the geometry of either site. Each spectrum shown in Figure 18 illustrate that the mutation has not disrupted either the T1 or the T2 copper sites. All samples prepared with only copper bound to the T1 site (the top three spectra (blue, red, and teal) in Figure 18) overlay well with each other and exhibit equivalent A_z and g_z-values which are listed in Table 8. The T2 copper signal also has equivalent A_z and g_z-values to that of the first generation model. As with the previous variants, the sum of the individual T1 copper and T2 copper spectra for the NiR3His variant are equivalent to the spectrum where both sites had been populated with copper.

Table 8: EPR parameters for the Phe15Trp second generation variants were estimated from the EPR spectra shown in Figure 18

Sample	A_z (G)	g_z
Free Cu	126	2.41
WT	62	2.24
WT Phe15Trp	62	2.25
NiR3His Phe15Trp T1Cu	58	2.24
NiR3His Phe15Trp T1Hg T2Cu	178	2.28

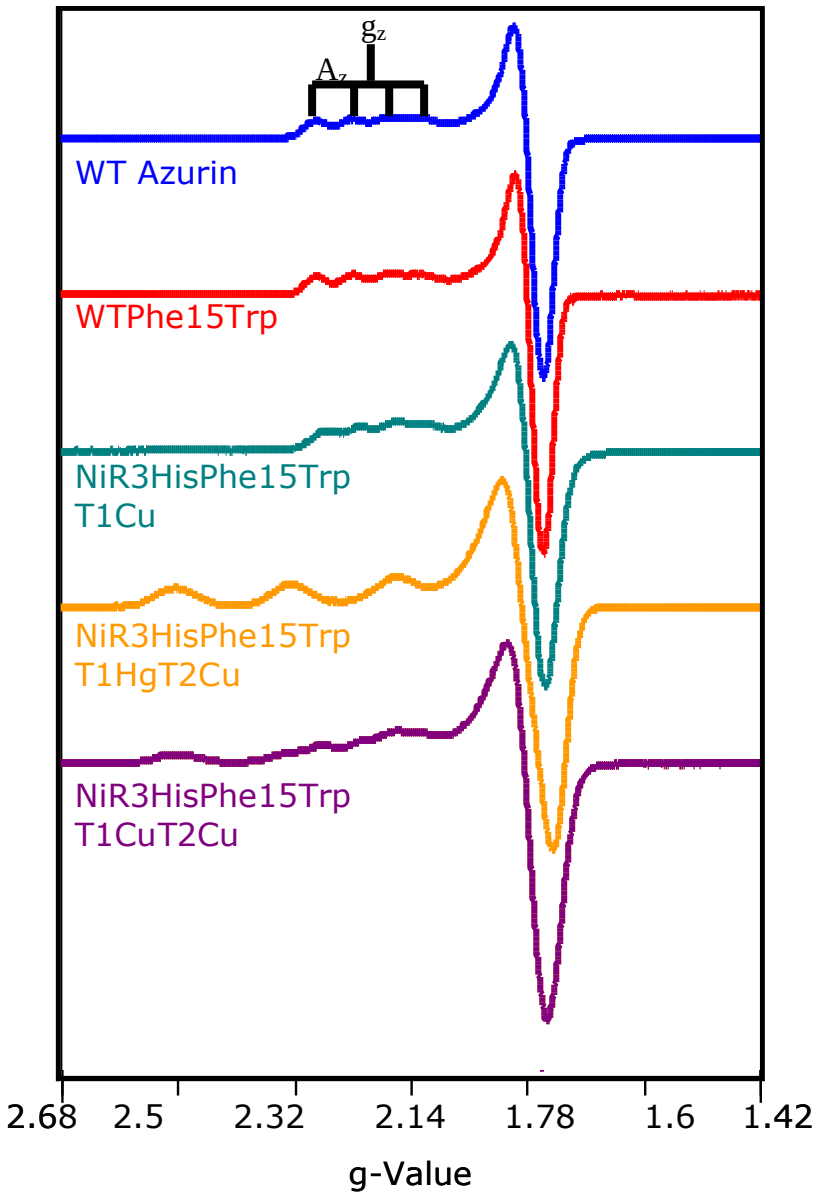

Figure 18: EPR spectra for the Phe15Trp variants are compared to free copper and wild type azurin. The corresponding parameters were previously shown in Table 8.

1.3.3 Reduction Potential of the 2nd Generation Models

Cyclic voltammetry of the three mutations on the wild type variants was completed to determine the change in potential as a result of the mutations. Three scans were run for each signal shown in Figure 19. The average deviation from the mean of the reduction potential determined from each of the three scans was ±5 mV for each variant. The reduction potential of both the WT→Phe114Pro and WT→Met121Gln variants was approximately 130 mV less than wild type azurin. The exact values are listed in Table 9. These two variants were intentionally designed to lower the potential of the T1 copper site so the cyclic voltammetry results confirm this was accomplished. The potential of the WT→Phe15Trp variant is about 20 mV lower than that of wild type azurin. This mutation was not intended to lower the potential, however previous research in our lab indicated that phenylalanine residues in the secondary coordination sphere increase the reduction potential by as much as 30 mV.[35] The removal of this phenylalanine must in turn decrease the potential by about the same, accounting for the 20 mV drop in potential.

Table 9: Reduction potential the T1 copper site experimentally determined from cyclic voltammetry signals shown in Figure 19.

Sample	Potential ±5 mV mV vs. NHE
WT-Azurin	**342 mV**
1) WTPhe114Pro	**211 mV**
2) WTMet121Gln	**216 mV**
3) WTPhe15Trp	**322 mV**

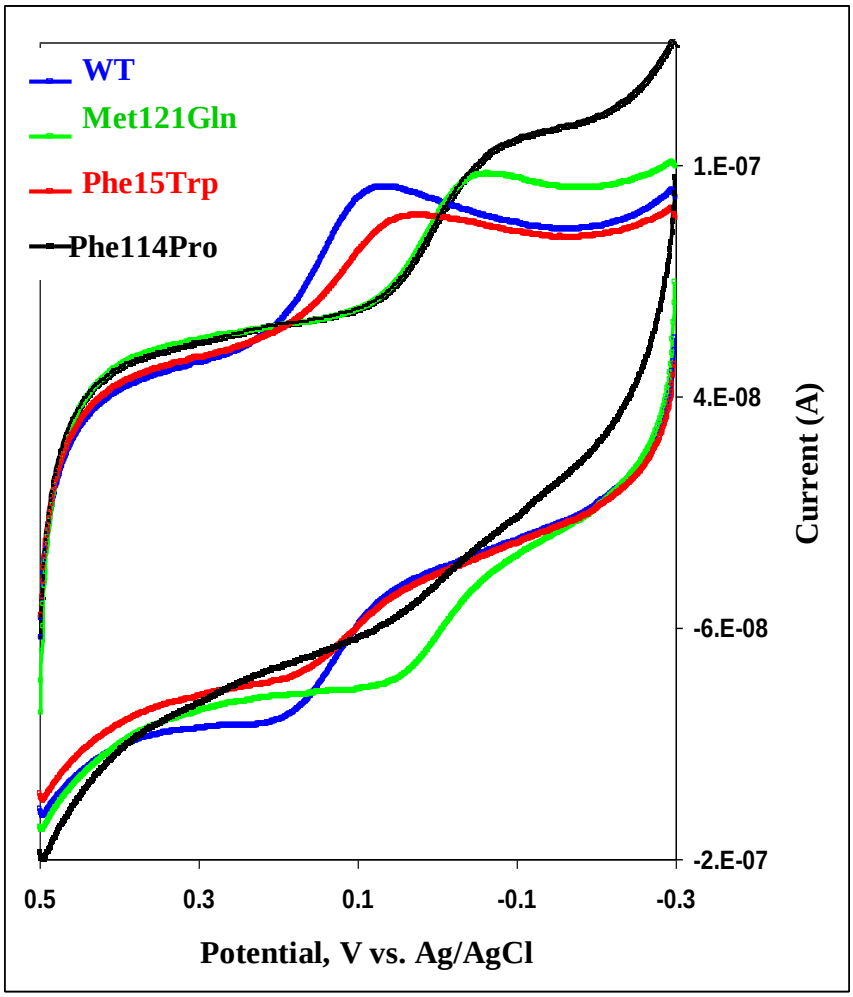

Figure 19: Cyclic voltammetry of the second generation azurin variants are overlaid and correspond to the reduction potentials reported in Table 9.

1.2.4 Griess Activity Assay

The activity of the first generation variants and the Az→NiR3His→Met121Gln second generation variant was measured with the Griess activity assay.[33] The activity of the other two second generation variants will be similarly measured in the future. The absorbance at 540 nm in Figure 20 is proportional to the concentration of substrate (NO_2^-) and decreases with the formation of product (NO). A second order reaction, $y = y_o / (y_o kt + 1)$, was used to fit each assay and determine the second order rate constant with respect to ascorbate concentration. These values along with the specific activity of the enzyme are listed in Table 10 along with the values determined for the first generation variants.

The specific activity of native NiR has been measured at 234 μmol of NO_2^- /min/mg enzyme.[39] The first generation Az→NiR3His activity was measured with the Griess activity assay at 7.68×10^{-3} μmol NO_2^- / min / mg enzyme which is 30,000 times slower than the native enzyme. The specific activity of Az→NiR3His→Met121Gln was measured with the Griess activity assay at 1.64×10^{-2} μmol NO_2^- / min / mg enzyme and 1.30×10^{-2} μmol NO_2^- / min / mg enzyme for two different assays. Each of these two reported values is the average of 3 individual assays done simultaneously. The average of the two Met121Gln assays (1.47×10^{-2} μmol NO_2^- / min / mg enzyme) is only 16,000 times less active than the native form as opposed to 30,000 times less active for the first generation variant.

The control reaction which does not contain any enzyme may be catalyzed by free ascorbate. The control reaction rate with the NiR3His variants is much faster than the control for NiR3His→Met121Gln. Several modifications to the assay have been

attempted to reduce this background reaction such as increasing the pH and completing the assay in the dark to reduce the formation of ascorbate radical. UV light creates free ascorbate radicals which would be capable of catalyzing the reaction; however assay results for the control which excluded light from the reaction were not significantly different than those in the presence of UV light. Increasing the pH was expected to slow down the reaction because the formation of product requires two protons and this would deplete the excess of protons in solution. The pH was increased from 5.5 to 5.6, however the rate of the control reaction did not significantly change as a result. More drastic pH changes will be made in the future to further attempt to reduce the ascorbate catalyzed reaction.

The native blue copper nitrite reductase is 30,000 times faster than the NiR3His variant, so the second generation variants were designed to increase the activity of the model. The Griess assay results for the Az→NiR3His→Met121Gln variant resulted in higher specific activity than the first generation models; however, the control run (without protein) with the second generation model was much faster than in the control run with the first generation variants. The first generation variants were assayed more than two years prior to the second generation variants, so slight conditional modifications may be responsible for the different control rates. After subtracting the rate constant for the control run with each assay to correct for this difference, the second generation variant is still 1.67 times more active than the first generation variant, however it is still 18,000 times less active than native NiR. The faster rate of the second generation variant indicates that reducing the potential of the T1 copper increases activity.

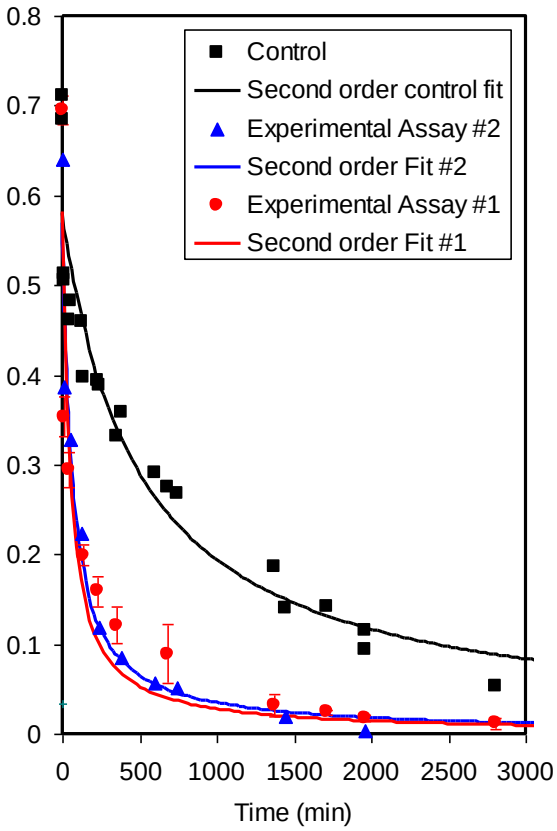

Figure 20: Griess Activity Assay with Az→NiR3His→Met121Gln
The average of three assay samples is represented by each data point and a second order reaction fit (represented by the solid lines) was used to determine the rate constant (k) reported in Table 10.

Table 10: Second order rate constants of both first and second generation variants derived from the fits represented in Figure 20 are reported along with their specific activity.

Second order Reaction	k (min^{-1})	Specific activity
Control with without enzyme	3.43E-03	1.72E-03 μmol NO_2^- min^{-1}
Assay #1 Az→NiR3HisMet121Gln 250 mM T1Cu T2Cu	3.43E-02	1.64E-02 (μmol NO_2^-)$(min)^{-1}$ $(mg\ Enz)^{-1}$
Assay #2 Az→NiR3HisMet121Gln 250 mM T1Cu T2Cu	2.73E-02	1.30E-02 (μmol NO_2^-)$(min)^{-1}$ $(mg\ Enz)^{-1}$
Average Met121Gln subtract control	2.74E-02	1.31E-02 (μmol NO_2^-)$(min)^{-1}$ $(mg\ Enz)^{-1}$
Control with w/o enzyme	1.30E-04	6.50E-05 (μmol NO_2^-)$(min)^{-1}$
Az→NiR3His 250 mM T1Cu T2Cu	1.61E-02	7.68E-03 (μmol NO_2^-)$(min)^{-1}$ $(mg\ Enz)^{-1}$
Az→NiR 250 mM T1Cu T2Cu	2.35E-03	1.12E-03 (μmol NO_2^-)$(min)^{-1}$ $(mg\ Enz)^{-1}$
WT-Az 250 mM T1Cu + 1 eq. Cu	3.51E-04	1.67E-04 (μmol NO_2^-)$(min)^{-1}$ $(mg\ Enz)^{-1}$
NiR3His subtract control	1.60E-02	7.62E-03 (μmol NO_2^-)$(min)^{-1}$

This assay will be repeated for the other two second generation variants. It is possible that the conformational changes resulting from the Met121Gln mutation may be responsible for the increased activity rather than the lower potential of the T1 site. If the Phe114Pro variant (which also lowers the potential of the T1 copper site) also has increased activity, this would support that tuning the reduction potential of the copper sites resulting in a more thermodynamically favored reaction increases the activity. Furthermore, hypothesis may be drawn that electron transfer between the two copper

sites is the rate limiting step because creating more thermodynamically favored potential difference between the two copper sites has increased the activity.

The Az→NiR3His→Phe15Trp variant will also be interesting to measure the activity. The more efficient pathway of electron transfer which is observed in native NiR is likely to be mimicked with the Phe15Trp variant. This is hypothesized to increase the activity.

1.4 Conclusions and Future Directions

Protein design is a rapidly developing field of biological chemistry. Our approach to protein design involves layering structural components, which are thought to be important for function, onto protein scaffold. In this way, we are uniquely able to individually test each layer for gain-of-function, as opposed to typical mutagenesis studies which look for loss-of-function.

The three second generation variants were individually layered onto five existing first generation models. The first generation Az→NiR3His variant had the most catalytic activity so it was chosen to study the effects of these layered mutations. Cyclic voltammetry for two second generation azurin variants, which were designed to lower the reduction potential of the T1 copper site, indicate that the potential of both were lowered by approximately 130 mV. Structural and spectroscopic similarities between the T1 site in the Phe114Pro variant and native blue copper NiR suggest this second generation variant is a better model than the first generation variant. This was not the case for the other reduction potential lowering variant Met121Gln. More structural and spectroscopic similarities exist between the T1 site in the Met121Gln variant and native green copper NiR. This suggests that the second generation variant Az→NiR3His→Met121Gln, may be a good model for green NiR. This model was particularly exciting because the activity of this variant was shown to be 1.67 times more active than the first generation model. The assay conditions still need to be modified to reduce the background reaction observed in the control. The activity of the other two second generation variants also needs to be measured with the Griess assay for comparison.

The second generation Az→NiR3His→Phe15Trp variant was not designed to lower the potential; however it was shown to decrease the reduction potential of the T1 copper site by approximately 20 mV. Phenylalanine mutations in the secondary coordination sphere of the T1 copper site have previously been shown to increase the potential, so it is logical that this mutation would slightly change the potential. The design was intended to create a more efficient physical pathway for the electron to transfer, however until the activity is measured, little insight into the effect of this layer of the design can be drawn.

Much still needs to be completed to determine the impact of these second generation variants. First, the EPR spectra needs to be simulated to obtain more accurate A_z and g_z - values. Second, a further analysis of the cyclic voltommetry by including the scan rate dependence of the current need to be measured to derive a diffusion coefficient. This will indicate that the signal is in fact from a large molecule (azurin). Third, the activity of the Phe114Pro and Phe15Trp variants need to be measured with the Griess activity assay to draw conclusions about whether or not enzyme activity increases with respect to a potential difference between the two copper sites and / or to the efficiency of the physical pathway the electron travels.

Furthermore, each of the primers for the second generation variants was intentionally designed so that they may be layered onto one another. For example, the addition of the Phe15Trp mutation on the Az→NiR3His→Phe114Pro is hypothesized to have more activity than any of the individual second generation variants. This hypothesis would be interesting to test in the future.

Another layer of structure function relationships may be addressed in the future with third generation variants. This would address the issue of substrate binding specificity. Incorporating more positively charged residues near the T2 copper binding site are hypothesized to attract the negatively charged nitrite substrate.

CHAPTER 2
PEPTIDYL GLYCINE α-HYDROXYLATING MONOOXYGENASE (PHM) MODELED IN AZURIN

2.1 Introduction

2.1.1 Peptidyl Glycine α-Hydroxylating Monooxygenase (PHM)

Peptidyl glycine α-hydroxylating monooxygenase (PHM) is a mammalian enzyme that uses molecular oxygen (O_2) and a reductant to catalyze the hydroxylation of substrate as shown in Figure 21.[40] PHM hydroxylates the α-carbon of a glycine residue neighboring a hydrophobic amino acid in the production of peptide hormones to prepare them for amidation by peptidylamidoglycolate lyase (PAL) as a posttranslational modification.[41] PHM and PAL are covalently linked to one another and this complex is commonly referred to as PAM.[41] The PAL complex is important to understand because amidated peptides may act as autocrine or paracrine growth factors to stimulate the proliferation of many types of cancer.[42]

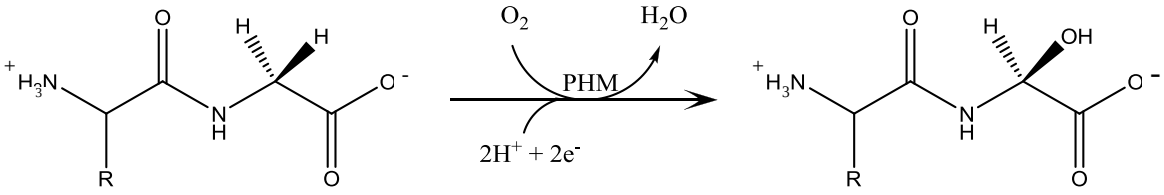

Figure 21: Catalytic Reaction of PHM (Scheme adapted from Evans *et. al*.) [43]

PHM contains two spectroscopically non-coupled copper ions separated by an 11.3 Å solvent-filled gap.[9] One copper center (called the Cu_H site) functions as the electron transfer site and the other is catalytically active (referred to as the Cu_M site).[40] The Cu_H electron transfer site is surrounded by a jelly roll motif, which is a combination

of two β-barrel Greek key motifs.[9] The catalytically active Cu_M site in PHM, composed of two antiparallel β-strands, is the location of oxygen binding and activation.[9] This catalytic site is located adjacent to a substrate-binding pocket.[43]

The mechanistic details of electron transfer between the two copper sites and α -hydroxylation of a peptide substrate are greatly debated, as are the nature of the reactive oxygen species and the order of electron transfer.[41, 44] Four previously proposed mechanisms for PHM have been proposed and are illustrated in Figure 22.[41, 43, 45]

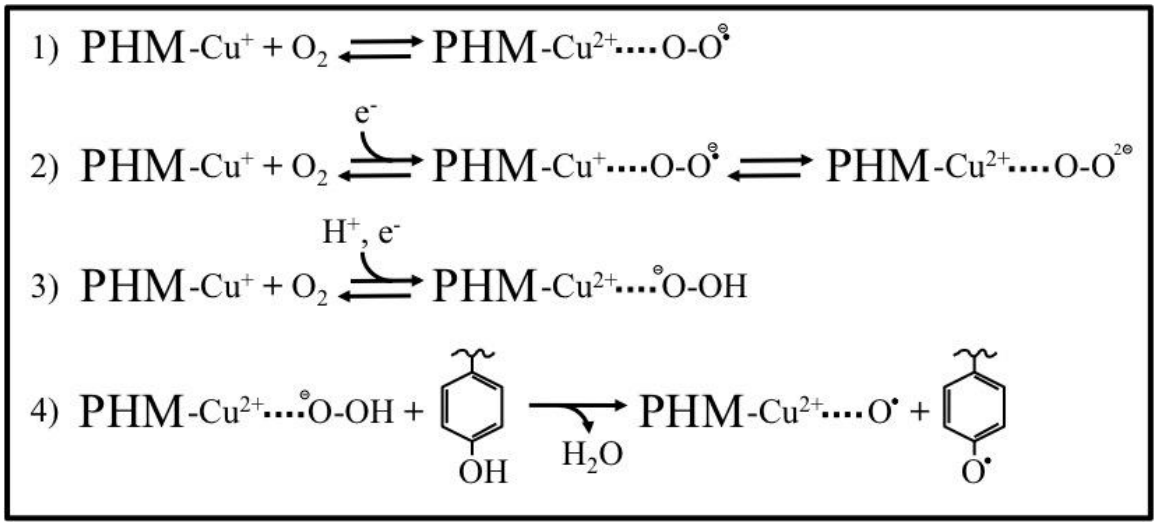

Figure 22: Four proposed mechanisms for PHM[43]
(Scheme adapted from Evans et. al.)

The first, proposes the Cu_M(I) donates one electron to O_2 to form the reactive oxygen species, $O_2\cdot^-$, that then abstracts a hydrogen atom.[43] The other electron is not transferred from the Cu_H(I) to the Cu_M(II) until after hydrogen abstraction.[43] The second mechanism proposes that Cu_H donates one electron to Cu_M(II)--O-O$\cdot^-$ complex forming a Cu_M(I) superoxo species.[43, 46] The now reduced Cu_M(I) donates another electron to the O-O$\cdot^-$ superoxo species forming Cu_M(II)--O-O^{2-}, or Cu(II) peroxo, which is the reactive

hydrogen atom abstracting species.[41] The third mechanism proposes that a copper hydroperoxide is the reactive oxygen intermediate.[47,43] The general concept is the same as for the second mechanism where both electrons are transferred prior to hydrogen abstraction, but in this case a proton is coupled with the second electron to form $Cu_M(II)$--O^- – OH.[47,43, 4] Other isotopic studies showed this was an unlikely intermediate with the substrate specific to PHM, so the fourth mechanism was proposed as an extension of this mechanism.[41, 43, 48] The fourth mechanism proposes that the $Cu_M(II)$hydroperoxide hypothesized by the third mechanism, undergoes reductive activation by a Tyr in the active site generating a copper-oxo species to abstract the hydrogen.[41, 49] Site specific mutagenesis studies showed that elimination of this Tyr318 had no effect on activity, so this mechanism is unlikely.[50,43]

The catalytically active species and the possible reaction intermediates are yet to be determined. Previous experimentation has reveled that a partially reduced dioxygen species accumulates and that both copper centers are oxidized before the substrate is activated, but the reactive oxygen intermediate is unknown.[41, 51] All four mechanisms agree that C_α-H cleavage is the first irreversible step and that a coordinating methionine ligand contributes to the stability of the reduced Cu_M site because the bond distance between copper and methionine is decreased in the reduced state.[41] The Cu_M site binds O_2 creating a reactive oxygen species capable of abstracting hydrogen after the substrate has bound.[41]

A number of synthetic copper complexes have been designed to model PHM which have elucidated the roles of the coordinating residues, the catalytically active

species, as well as the plausible reaction intermediates.[12] Using azurin as a protein scaffold distinguishes it from the previous synthetic models.

2.1.2 Construction of the Protein-Based Model of PHM

A better understanding of the electron transfer and mechanism of PHM may be gained from modeling the dinuclear copper center in azurin.[9] Azurin is a T1 class of copper proteins and it functions in electron transfer, similar to the Cu_H site in PHM.[9] No other copper sites exist in azurin; however there is a β-sheet motif similar to PHM, making azurin ideal for the design of a second copper site.[9]

The Berry lab group previously created two models for PHM which will be referred to as Az→PHM, and Az→PHM3His. This modeling was accomplished first by maintaining the T1 copper site in azurin (circled with a solid line in Figure 23a) which will model the electron transfer Cu_H site of native PHM (circled with a solid line in Figure 23b). Second, the β-sheet of azurin was mutated (dashed circle in Figure 23a) to mimic the T2 (Cu_M) site in PHM (dashed circle in Figure 23b).[9]

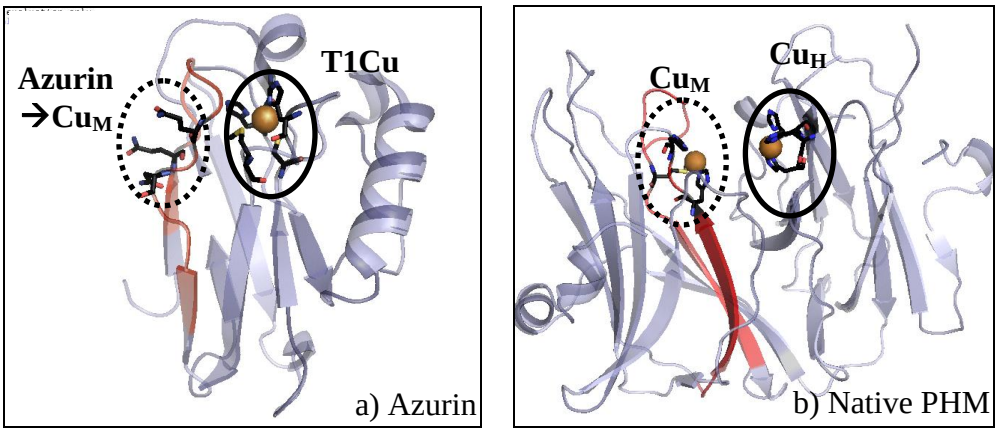

Figure 23: The electron transfer site in each protein is circled with a solid line while the catalytic site (the modeled PHM catalytic site in azurin) is circled with a dotted line. a) Wild type azurin (PDB: 4AZU) rendered with Pymol b) Native PHM (PDB: 1PHM) rendered with Pymol

The separation between the T1 copper and the modeled Cu_M sites was estimated between 11 and 13 Å, similar to the distance between the copper sites in native PHM.[9] The Berry lab group previously created two models for PHM which will be referred to as Az→PHM, and Az→PHM3His. Three ligands are (circled with a dashed line in Figure 23a)**,** Gln8Met, Gln14His, and Asn16His were mutated in azurin to mimic the PHM catalytic site. This variant was named Az→PHM3His. The difference between the two models created, is the mutation of Gln8 to histidine in the Az→PHM3His model rather than methionine in the Az→PHM model. Comparison of the two models will indicate the importance of the methionine ligand for the catalytic reaction.[9] This mutagenesis was completed without disrupting the existing T1 copper electron transfer center.

Construction of the azurin variants was accomplished through Stratagene Quikchange mutagenesis, a procedure which was previously discussed in more detail in section **1.2.1** of this thesis. Mutation of the three amino acids in azurin was achieved with a single pair of primers in one round of mutagenesis for each variant.[9] The gene was successfully over-expressed in *E. coli* in relatively high yields (~20 mg azurin per liter of cell culture).[9]

ESI mass spectroscopy provided evidence for both models that the T1 site has been undisturbed by building the T2 site, and that the modeled T2 site binds copper.[9]

2.2 Methods

2.2.1 X-Band EPR Spectroscopy

EPR spectroscopy, simulation of the spectra, and reduction experiments on the EPR samples were completed. Each of these EPR samples were prepared and run as outlined in sections **1.2.2** and **1.2.3** of this thesis.

2.2.2 Reduction and Recovery of Oxidized Copper Centers

Recovery time of the oxidized state of each copper site in Az→PHM and Az→PHM3His was monitored by reducing the EPR samples to Cu(I) and observing as these samples were oxidized by O_2 back to Cu(II) by slowly dissolving oxygen from the atmosphere into each sample. EPR samples were prepared as in section **1.2.2**; however, more than four EPR samples for a total of 650 μL of 2 mM protein were combined prior to adding glycerol. These combined samples were placed in one 1.2 μL flat bottom screw cap tube and stirred at 4° C exposed to the atmosphere. A 150 μL aliquot was removed and diluted to 1 mM with glycerol for the oxidized sample prior to adding reductant. A ten fold excess of freshly prepared ascorbate in 50 mM ammonium acetate pH 5.1 was then added to reduce the remaining sample in the screw cap tube while stirring at 4° C. The volume change as a result of adding reductant was minimized by using a more concentrated ascorbate stock (1000 mM) so that only 10 μL of ascorbate would be added to the 500 μL sample. The sample turned from bright blue to clear after the ascorbate had reduced the copper centers and another 150 μL aliquot was removed, diluted to 1 mM with glycerol and frozen to run EPR. This was called the reduced sample. The first "recovery" sample was removed and diluted in glycerol as soon as a faint blue color

began to return to the solution. The time for this recovery typically varied between one and ten hours. The last recovery sample was taken when bright blue color returned or after 5 days. All samples were stored in EPR tubes and submerged in liquid nitrogen until EPR spectroscopy could be completed on all the samples. Parameters for these samples were identical to those listed in section **1.2.3** of this thesis.

2.3 Results and Discussion

2.3.1 X-Band EPR

The protein-based model allows for the spectroscopic isolation of each site with EPR (Figure 24). The spectroscopic isolation of the T1 site is accomplished by binding 1 equivalent of copper (which preferentially binds the T1 site) and then removing excess copper by running the sample down a PD-10 desalting column (the top spectra for each of the two models in Figure 24). The T2 site is isolated by first binding Hg(II) which is spectroscopically silent to the T1 site (the second spectra in Figure 24) and then titrating copper which will populate the T2 site with copper (the third spectra in Figure 24). It is not possible to spectroscopically isolate these sites in native PHM because both sites have similar binding affinities for both copper and mercury. The bottom spectra in Figure 24 represent copper bound to both sites and are similar to the EPR spectra observed for native PHM. Obtaining clear EPR spectra is important for understanding the geometry of the modeled T2 (Cu_M) site. Figure 24 provides an example of the EPR data collected for both the Az→PHM and Az→PHM3His models

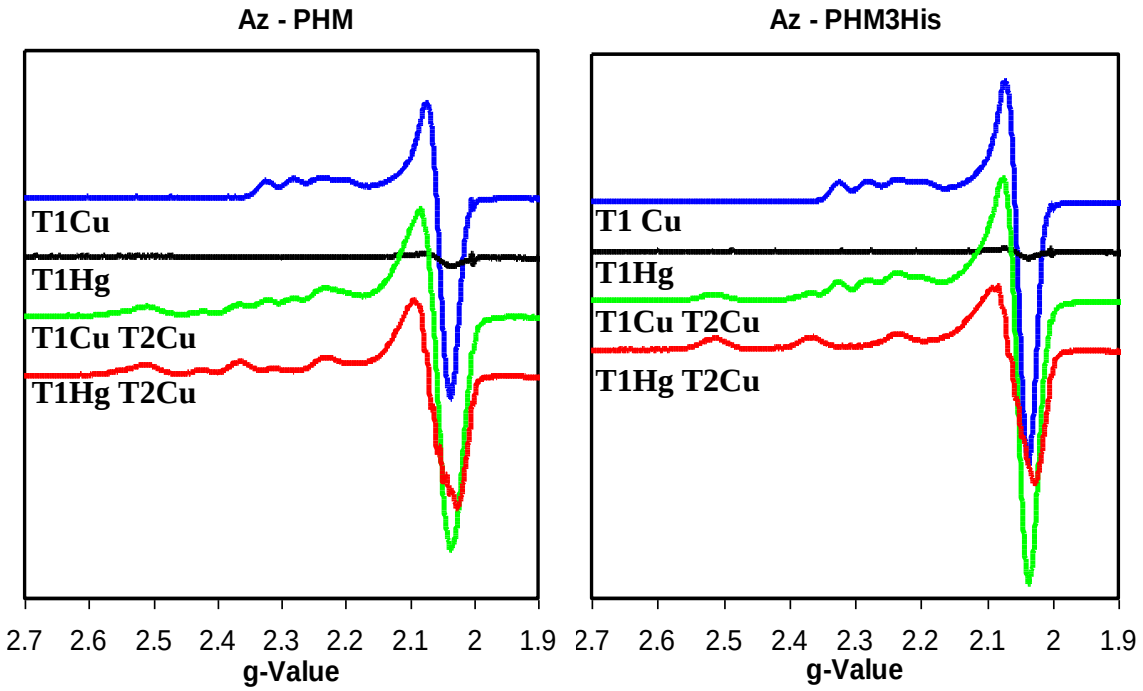

Figure 24: EPR spectra for the two PHM models which use azurin as scaffold (Az→PHM shown left and Az→PHM3His shown right). The top EPR spectrum in blue for both models is with copper bound to the T1 electron transfer site. The second spectrum (black) is with mercury bound in the T1 site and is expected to have no signal because Hg^{+2} does not have an unpaired electron. The third spectrum (green) has copper bound in both sites and is expected to be the sum of both the blue and the red spectrum. The red spectrum at the bottom has Hg^{+2} bound to the T1 site so that copper in the T2 site may be observed separately.

SIMPOW6 software was used to simulate the spectrum of the T1 and T2 copper sites of both the PHM models.[30] The expected spectrum for copper bound in both sites is the addition of the T1 copper spectrum to the T2 copper spectrum. The two simulated spectra were added together and overlaid with the experimentally observed spectrum with both copper sites populated (Figure 25). Minimal deviations are shown between the simulated and experimental spectra for Az→PHM3His in Figure 25. The simulations provided accurate A_z-value and g_z-values for each of the spectra. It was remarkable that the EPR parameters for the Az→PHM variant model literature values for native PHM.[30,40]

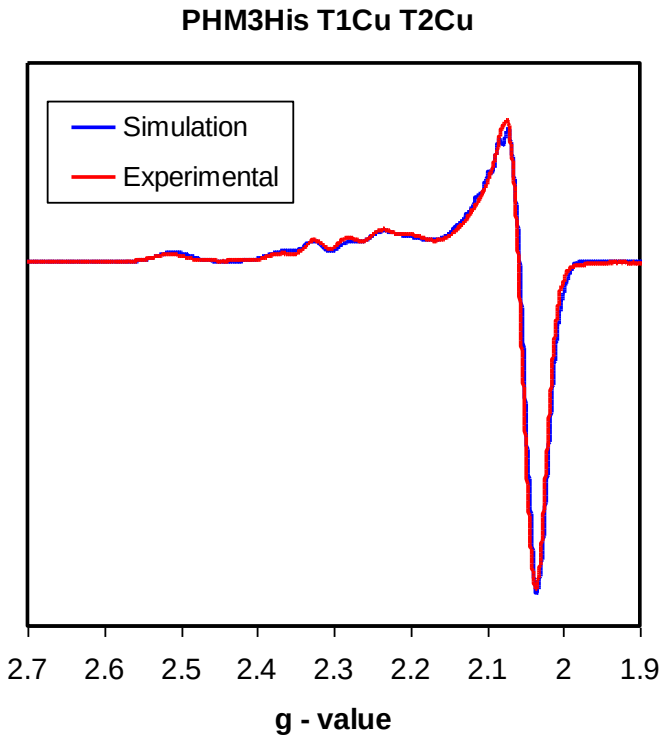

Figure 25: Overlay of simulated[30] EPR data with the experimentally observed spectrum for Az→PHM3His

2.3.2 Reduction and Recovery of Oxidized Copper Centers

These experiments lacked reproducibility; however the data shown is overall representative of the 18 total experiments completed. Concentration dependence studies provided evidence that 0.02 mM or more fluctuations in concentration between individual experiments affected the recovery time. The samples were initially diluted in glycerol and separated into individual tubes prior to reducing each sample. This initial method was modified to the method discussed in section 1.2.2, because glycerol was shown to increase the recovery time and the new method reduced small fluctuations in concentration. These experimental modifications increased reproducibility of the results.

EPR data was collected for the both PHM-Az and PHM3His-Az with copper bound to both sites (Figure 26). Following reduction of both sites with ascorbate, the T2 copper site recovers faster than the T1 site. This may indicate that if the T1 site is oxidized by oxygen, it is then reduced by the T2 copper. The other possibility is that the T2 site is more exposed to solvent than the type one site, so it is more probable to get oxidized by oxygen in solution. It may also reflect the difference in reduction potential of the two copper sites, because the T1 Cu potential is higher, so it is more likely to be reduced.

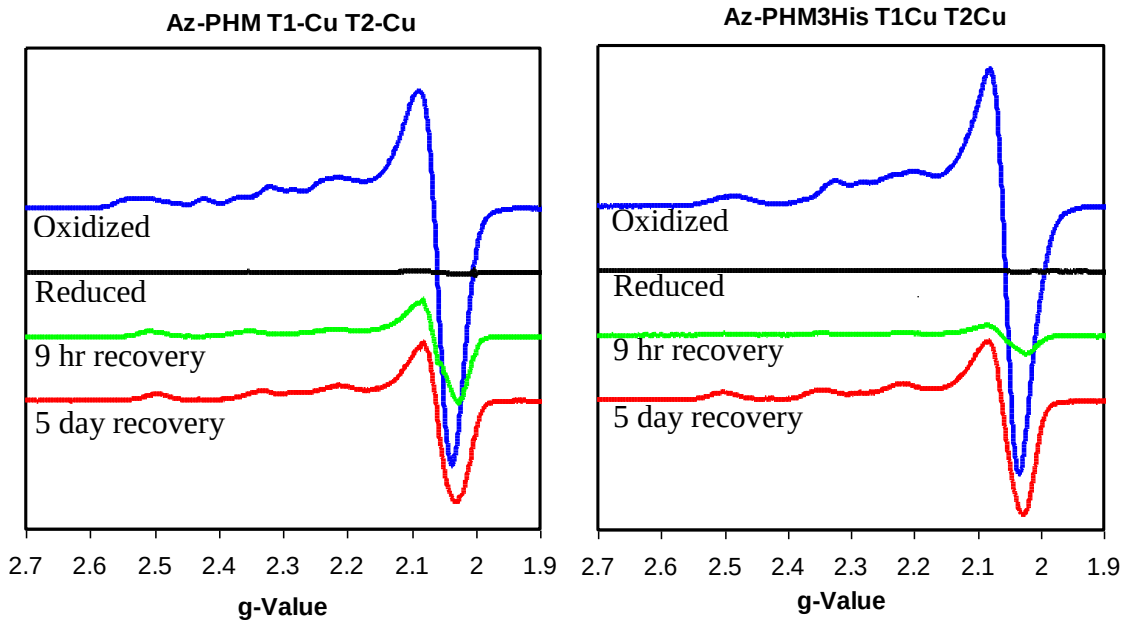

Figure 26: Recovery of the oxidized copper centers following reduction with ascorbate. Initially both sites were in the oxidized Cu(II) state (blue). Following from top to bottom, spectra (black) were collected after reduction to Cu(I), initial recovery (green) to the oxidized state, and final recovery (red) back to Cu(II).

The recovery experiment was also completed on both models with mercury in the T1 site and copper in the T2 site. It is unlikely that mercury would give up an electron to copper because it has a d^{10} electron configuration so it is very stable in the Hg(II) oxidation state. If the T1 copper were donating its electron to the T2 copper in the previous experiment, the recovery time for the T1Hg T2Cu sample would be slower than for the samples with copper in both sites; however, this was not observed. The T2 site was close to being completely re-oxidized after only 1.5 hours with mercury in the T1 site (Figure 27) as opposed to more than 9 hours with copper in both sites (Figure 26).

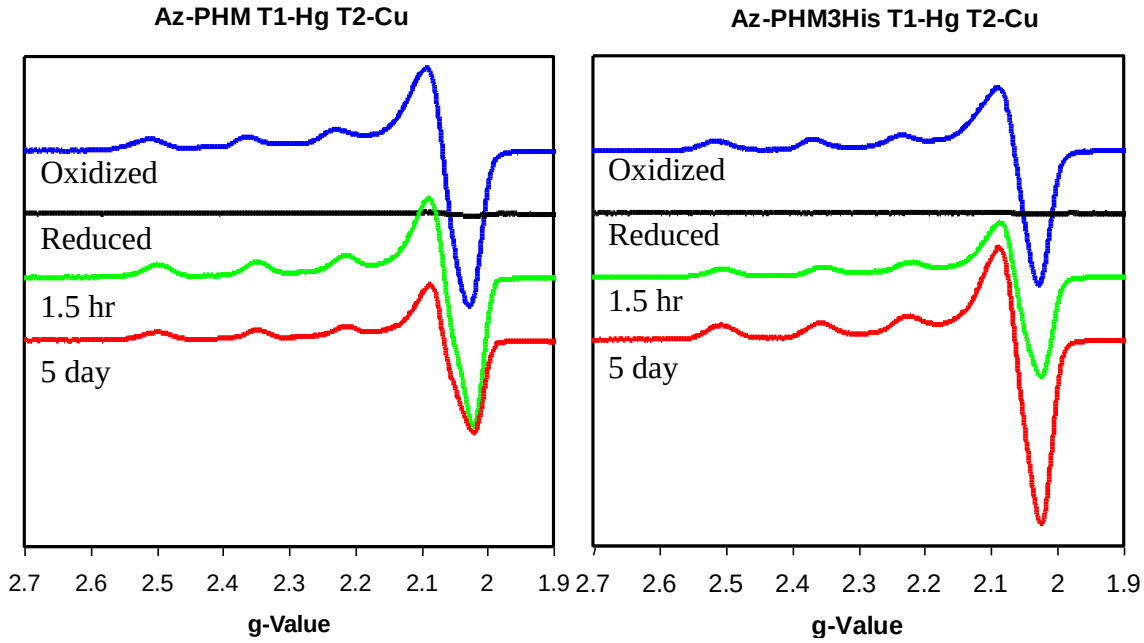

Figure 27: Recovery of the oxidized T2 copper centers following reduction with ascorbate. Initially the type two site was oxidized Cu(II) shown in blue. Following from top to bottom, spectra (black) were collected after reduction to Cu(I), initial recovery (green) to the oxidized state, and final recovery (red) back to Cu(II).

In some experiments, the protein never fully recovered or showed a weaker signal after 5 days. This is most likely due to denaturation caused by stirring while exposed to the atmosphere for 5 days. The sulfur from Cys112 which coordinates the T1 copper also may undergo oxidation with this experiment which may result in the T1 copper dissociating from the T1 site. This is unlikely because free copper would have been observed in the EPR signal if this were the case. Other control experiments with only T1 copper bound fully recovered after 15 hours. This indicates that the lack of exposure to solvent is inhibiting the oxidation of this site rather than an electronic communication with the T2 copper.

2.4 Conclusions and Future Directions

The models constructed previously by the Berry lab group were successfully characterized with EPR spectroscopy. They have shown to be good spectroscopic models of native PHM, however structure and function relationships of PHM were not elucidated through studying the models with the recovery experiments as hoped. The faster recovery time observed with mercury bound in the T1 site rather than copper does not necessarily indicate electronic communication is occurring between the two copper centers. It is likely that the T2 site is more rapidly oxidized either because it is more solvent exposed than the T1 copper, or because it has a lower reduction potential and is therefore more likely to be oxidized than the T1 copper.

Repeating these experiments with substrate present would shed light on whether or not substrate binding promotes oxidation. Optimizing the reproducibility of these experiments will be important for any major conclusions drawn with substrate present.

The next step to take with these models is to complete an activity assay to demonstrate the model is not only structurally similar to native PHM, but also functionally similar. Steps towards developing this assay have been made which utilize an oxygen sensor to monitor oxygen consumption with and without substrate present. Second generation models for PHM are also being constructed; however they have not yet been characterized or studied. These models were discussed in Chapter 1 extensively.

CHAPTER 3
CYCLIC VOLTAMMETRY WITH NATIVE TYRAMINE β-MONOOXYGENASE

3.1 Introduction

Tyramine β-monooxygenase (TBM) is an enzyme found in invertebrates and catalyzes the hydroxylation of tyramine to octopamine.[52] TBM is structurally analogous to the mammalian enzyme PHM; however, PHM hydroxylates glycine, not tyramine.[52] While not all invertebrate nerve cells contain TBM, both the reactant and the product of TBM are neurotransmitters.[53] It is unclear whether or not nerve cells devoid of TBM only release tyramine, so a further understanding of TBM would add to our understanding of the nervous system.[53]

The reduction potential of TBM has not been directly measured, so the Judith P. Klinman lab group (UC Berkley) who studies TBM is collaborating with the Berry lab group to conduct direct cyclic voltammetry. We are excited to report a direct cyclic voltammetry signal for TBM. The cyclic voltammetry was measured both for TBM with a histidine purification tag attached, and after its removal. The diffusion coefficient was also derived from the experiment to indicate that the signal is from a large molecule (protein) and that the electrochemical signal was diffusion controlled.[54]

3.2 Methods

The Klinman lab group initially provided TBM protein purified from *Drosophila* with a histidine tag used for the purification attached.[52] The sample preparation and scanning conditions were optimized before running cyclic voltammetry on TBM without the His tag because the removal of the His tag results in lower purification yields. The optimized sample preparation for the scans shown in Figure 28 were prepared from a 0.6 mM TBM sample in 50 mM potassium phosphate buffer pH 7. A buffer exchange to 100 mM NaCl, 50 mM Tris pH 7.5 was completed with a PD-10 desalting column. This buffer exchange resulted in a 0.036 mM TBM sample to which 5 equivalents of $CuSO_4$ (from a 10 mM stock solution) were added slowly, one quarter of an equivalent at a time. The solution was concentrated with a 10 kDa exclusion membrane to 0.2 mM while spinning at 5000 rpm, 4° C. Excess copper was removed by diluting this sample to 0.02 mM, concentrating again, and repeating for a total of three concentration spins. This sample was scanned at variable scan rates to derive the diffusion coefficient from the dependence of the cathodic peak current on the scan rate. The working electrode was a pyrolytic graphite edge electrode polished with 0.05 micron alumina powder. The reference electrode was a standard calomel electrode rather than the Ag / AgCl reference usually used because control scans run with buffer showed that a precipitate was formed with the Tris buffer which was not a problem with the calomel electrode. The counter electrode was a platinum wire and the sample was scanned at 20° C under argon gas.

This procedure was repeated for the His tag deleted protein sample, however due to issues with protein precipitation and having a smaller protein stock, the final concentration of the His tag deleted sample was only 0.077 mM.

3.3 Results and Discussion

Cyclic voltammetry scans (shown in Figure 28 for the 50 mV/s scan rate) were measured for TBM with and without the histidine purification tag. Only one cathodic and one anodic peak were observed for both of the non-coupled dinuclear copper atoms. The average reduction potential of TBM for all the measured scan rates with the His tag attached was 224.2 ± 7.4 mV and without the His tag the potential was 234.2 ± 6.8 mV. These potentials are within error of one another indicating that the signal may not be from copper bound to the His tag, but rather from the two copper sites in the protein. The potential of native TBM has never been measured; however both copper sites are classified as T2 coppers so it is reasonable they would both have similar potentials. T2 copper sites usually have a lower potential than T1copper sites and the measured TBM potential is more than 100 mV less than the T1 copper site in azurin.

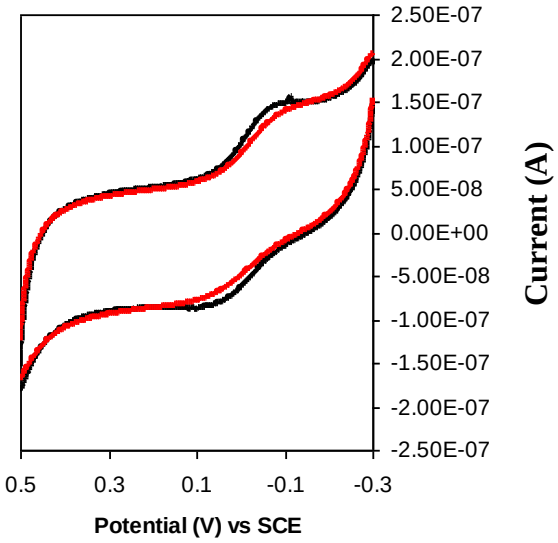

Figure 28: Cyclic voltammetry scanned at 50 mV/s for TBM with the His tag attached (shown in red) is overlaid with TBM without the His tag (black)

Separation between the anodic and cathodic peaks varied between 112 mV and 175 mV which are larger than the peak separations seen in wild type azurin between 60 mV and 100 mV. TBM is a larger protein which would be expected to diffuse slower and thus have larger peak separations. The trends outlined by Figure 29 show that as the scan rate increases, so does the peak separation indicating a direct electrochemical signal. The change in potential as a function of scan rate (the slope of the bottom two trends shown in Figure 29) for the anodic peak is expected to be equal and opposite to that of the cathodic peak. This would indicate that the midpoint (reduction potential) is constant regardless of the scan rate, which is the case for the TBM sample with the His tag still attached (Figure 29 (a)). The slope for the anodic peak current of the TBM sample without the His tag is much less than the magnitude of the cathodic peak. The difference between these trends is most likely a result of the lower concentration of the TBM sample without the His tag (Figure 29b).

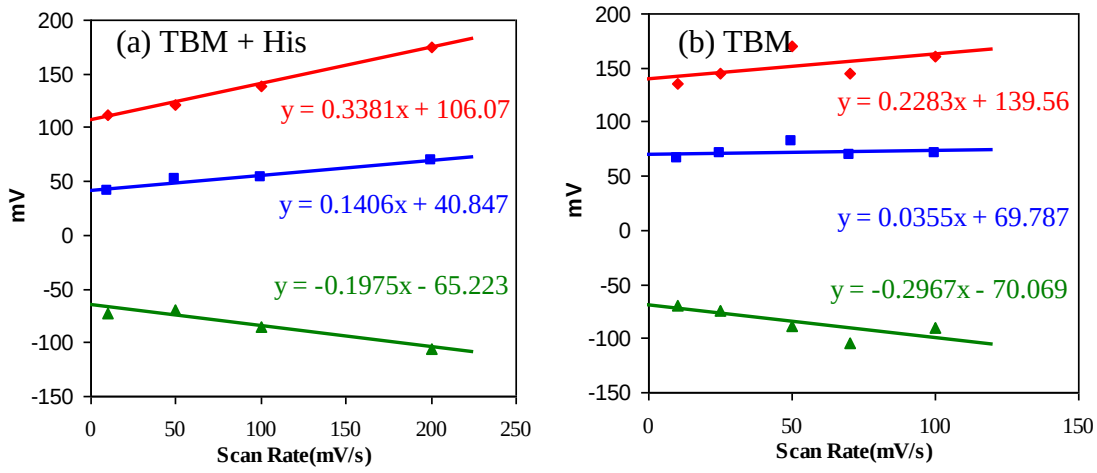

Figure 29: Cyclic Voltammetry peak trends for (a) TBM with the His purification tag attached and (b) TBM without the His purification tag.

The relationship between the scan rate (ν) and cathodic peak current (i_p) is represented with Equation 2.[35] The slopes of the Figure 30 plots were used as to derive the diffusion coefficients of the protein to the electrode from the cyclic voltammetry signals using Equation 2.[35]

$$i_p = 0.4463nFAC \sqrt{(nF/RT)} \sqrt{D} \sqrt{\nu} \qquad \text{Equation [2]}$$

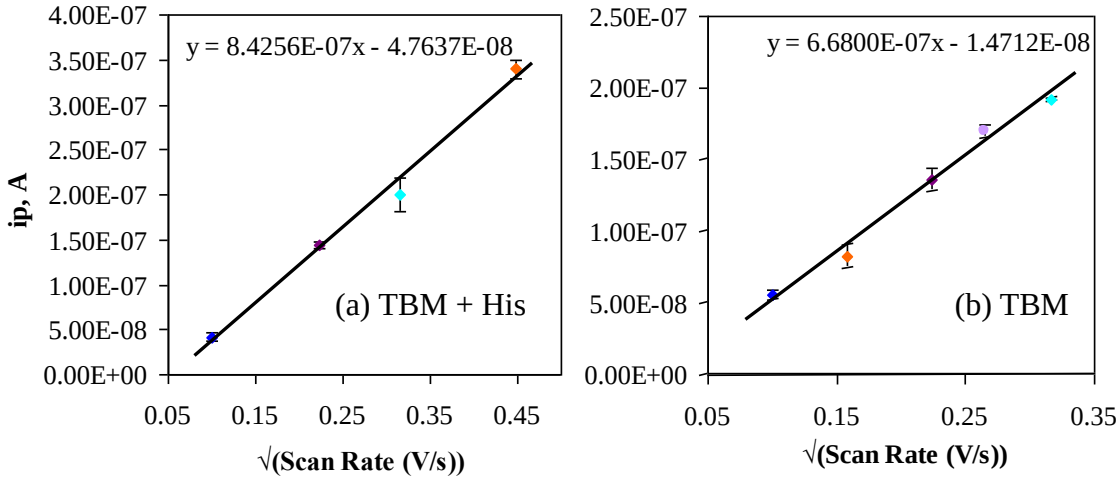

Figure 30: Cathodic peak current dependence on √(scan rate)
(a) TBM with the His purification tag
(b) TBM after removal of the His purification tag

The diffusion coefficients (shown in Table 11) derived from the relationship between the scan rate and cathodic peak current were comparable to proteins with similar molecular weights. This method was used to determine the diffusion coefficient for both TBM samples; however, it is dependent on concentration which explains the variance between the two. The diffusion coefficient for TBM with the His tag attached is 1.94 x 10^{-6} cm^2/s which is logical because TBM (68,580 Da) is a larger protein than azurin larger molecules diffuse slower. The diffusion coefficient of wild type azurin (14,000 Da)

was previously determined with this method as 3.78 x 10^{-6} cm^2/s which is similar to the known diffusion coefficient for Cytochrome c (13,400 Da) which is 1.16 x 10^{-6} cm^2/s.[54] The diffusion coefficient for bovine hemoglobin (68,000 Da) which has a similar molecular weight is 7.32 x 10^{-7} cm^2/s. The faster diffusion coefficient calculated for TBM after removal of the His tag (D = 4.63 x 10^{-6} cm^2/s) is most likely a result of the lower concentration of this sample or due to having polished the electrode between scans, so the results need to be repeated. This analysis supports that the cyclic voltammetry signals were from a large, slowly diffusing molecule (protein), rather than from smaller molecules such as free copper or buffer. It also suggests that the electrochemical process is diffusion controlled, as opposed to protein film electrochemistry where the protein is bound to the electrode surface.[38]

Table 11: Diffusion coefficients calculated from Equation 2.

	WT Azurin	**TBM + His**	**Error**	**TBM**
Slope (A√(s/V))	5.747E-07	8.42563E-07	6.01E-08	6.67996E-07
A = Electrode Area (cm^2)	0.011	0.015	0.001	0.0077
C = Protein Concentration (mmol/L)	1 mM	1.5 mM	0.1mM	0.77 mM
T = Temperature (K)	298	298	2	298
R = Gas constant J/(mol*K)	8.314472	8.314472		8.314472
D = Diffusion Coefficient (cm^2/s)	3.78016E-06	1.94E-06		4.6323E-06

Many other controls such as scans with $CuSO_4$ or scans with Na_2SO_4 were completed which confirmed that the signals for TBM were not that of free copper or free sulfate in solution.

3.4 Conclusion and future directions

The average reduction potential of TBM for all the measured scan rates with the His tag attached was 224.2 ± 7.4 mV and without the His tag the potential was 234.2 ± 6.8 mV. These potentials are within error of one another and support that the signal is not from copper bound to the His tag, but rather from the two copper sites in the protein. The potential of native TBM has never been measured; however both copper sites are classified as T2 coppers so it is reasonable they would both have similar potentials

The diffusion coefficient was derived from the dependence of the cathodic peak current on scan rate which verified that the signal was from a large molecule (protein) and that the electrochemical signal was diffusion controlled. Variation between the sample which still had the histidine purification tag attached and the sample which did not, are most likely a result of concentration differences between the samples or from polishing the electrode differently. The precipitation problems resulting from binding copper to the His deleted TBM resulted in difficulty preparing a large enough sample to complete cyclic voltammetry at the same concentration. Cyclic voltammetry will be repeated for a larger sample of the TBM without the His purification tag at the exact same scan rates as for the TBM + His tag upon receiving a larger sample from the Klinman lab group. The sample will subsequently be analyzed with EPR to verify copper binding. For the first time with direct cyclic voltammetry, we report that the reduction potential of both TBM copper sites is between 224 mV and 234 mV.

REFERENCES

1. Jetten Mike, S. M., The microbial nitrogen cycle. *Environ Microbiol* **2008,** *10* (11), 2903-9.

2. Beckman, J. S.; Beckman, T. W.; Chen, J.; Marshall, P. A.; Freeman, B. A., Apparent hydroxyl radical production by peroxynitrite: implications for endothelial injury from nitric oxide and superoxide. *Proc. Natl. Acad. Sci. U.S.A.* **1990,** *87* (4), 1620-4.

3. Zumft, W. G., Cell biology and molecular basis of denitrification. *Microbiology and Molecular Biology Reviews* **1997,** *61* (4), 533-616.

4. Dodd, F. E.; van Beeumen, J.; Eady, R. R.; Hasnain, S. S., X-ray structure of a blue-copper nitrite reductase in two crystal forms. The nature of the copper sites, mode of substrate binding and recognition by redox partner. *J. Mol. Biol.* **1998,** *282* (2), 369-382.

5. Bertini, I.; Gray, H. B.; Lippard, S. J.; Valentine, J. S., *Bioinorganic Chemistry*. University Science Books: Sausalito, CA, 1994; p 611.

6. Morozkina, E. V.; Kurakov, A. V., Dissimilatory nitrate reduction in fungi under conditions of hypoxia and anoxia: A review. *Applied Biochemistry and Microbiology* **2007,** *43* (5), 544-549.

7. Godber, B. L. J.; Doel, J. J.; Goult, T. A.; Eisenthal, R.; Harrison, R., Suicide inactivation of xanthine oxidoreductase during reduction of inorganic nitrite to nitric oxide. *Biochem. J.* **2001,** *358* (2), 325-333.

8. Koteishi, H.; Nojiri, M.; Nakagami, T.; Yamaguchi, K.; Suzuki, S., Cytochrome c551 is a mediator of electron transfer between copper-containing nitrite reductase and azurin in a denitrifying bacterium, Achromobacter xylosoxidans. *Bull. Chem. Soc. Jpn.* **2009,** *82* (8), 1003-1005.

9. Berry, S. M.; Mayers, J. R.; Zehm, N. A., Models of noncoupled dinuclear copper centers in azurin. *J. Biol. Inorg. Chem.* **2009,** *14* (1), 143-149.

10. Strange, R. W.; Murphy, L. M.; Dodd, F. E.; Abraham, Z. H. L.; Eady, R. R.; Smith, B. E.; Hasnain, S. S., Structural and Kinetic Evidence for an Ordered Mechanism of Copper Nitrite Reductase. *J. Mol. Biol.* **1999,** *287* (5), 1001-1009.

11. Schneider, J. L.; Carrier, S. M.; Ruggiero, C. E.; Young, V. G., Jr.; Tolman, W. B., Influences of Ligand Environment on the Spectroscopic Properties and Disproportionation Reactivity of Copper-Nitrosyl Complexes. *J. Am. Chem. Soc.* **1998,** *120* (44), 11408-11418.

12. Tolman, W. B., Using synthetic chemistry to understand copper protein active sites: a personal perspective. *J. Biol. Inorg. Chem.* **2006,** *11* (3), 261-271.

13. Merkle, A. C.; Lehnert, N., The Side-On Copper(I) Nitrosyl Geometry in Copper Nitrite Reductase Is Due to Steric Interactions with Isoleucine-257. *Inorg. Chem.* **2009,** *48* (24), 11504-11506.

14. Yokoyama, H.; Yamaguchi, K.; Sugimoto, M.; Suzuki, S., CuI and CuII complexes containing nitrite and tridentate aromatic amine ligand as models for the substrate-binding type-2 Cu site of nitrite reductase. *Eur. J. Inorg. Chem.* **2005,** (8), 1435-1441.

15. Sutherland, I. W.; Wilkinson, J. F., Azurin: a copper protein found in Bordetella. *J. Gen. Microbiol.* **1963,** *30*, 105-12.

16. Prudencio, M.; Eady, R. R.; Sawers, G., The blue copper-containing nitrite reductase from Alcaligenes xylosoxidans: cloning of the nirA gene and characterization of the recombinant enzyme. *J. Bacteriol.* **1999,** *181* (8), 2323-2329.

17. Solomon, E. I.; Penfield, K. W.; Gewirth, A. A.; Lowery, M. D.; Shadle, S. E.; Guckert, J. A.; LaCroix, L. B., Electronic structure of the oxidized and reduced blue copper sites: contributions to the electron transfer pathway, reduction potential, and geometry. *Inorg. Chim. Acta* **1996,** *243* (1-2), 67-78.

18. Solomon, E. I., Spectroscopic Methods in Bioinorganic Chemistry: Blue to Green to Red Copper Sites. *Inorg. Chem.* **2006,** *45* (20), 8012-8025.

19. Murphy, M. E. P.; Turley, S.; Adman, E. T., Structure of nitrite bound to copper-containing nitrite reductase from Alcaligenes faecalis. Mechanistic implications. *J. Biol. Chem.* **1997,** *272* (45), 28455-28460.

20. Marcus, R. A.; Sutin, N., Electron transfers in chemistry and biology. *Biochim. Biophys. Acta* **1985,** *811*, 265-322.

21. Berry, S. M.; Bladholm, E. L.; Mostad, E. J.; Schenewerk, A. R., Incorporation of the red copper nitrosocyanin binding loop into blue copper azurin. *J. Biol. Inorg. Chem.* **In Press**.

22. Leferink, N. G. H.; Han, C.; Antonyuk, S. V.; Heyes, D. J.; Rigby, S. E. J.; Hough, M. A.; Eady, R. R.; Scrutton, N. S.; Hasnain, S. S., Proton-coupled electron transfer in the catalytic cycle of Alcaligenes xylosoxidans copper-dependent nitrite reductase. *Biochemistry* **2011,** *50* (19), 4121-4131.

23. Marshall, N. M.; Garner, D. K.; Wilson, T. D.; Gao, Y.-G.; Robinson, H.; Nilges, M. J.; Lu, Y., Rationally tuning the reduction potential of a single cupredoxin beyond the natural range. *Nature* **2009,** *462* (7269), 113-116.

24. Yanagisawa, S.; Banfield, M. J.; Dennison, C., The Role of Hydrogen Bonding at the Active Site of a Cupredoxin: The Phe114Pro Azurin Variant. *Biochemistry* **2006,** *45* (29), 8812-8822.

25. Romero, A.; Hoitink, C. W. G.; Nar, H.; Huber, R.; Messerschmidt, A.; Canters, G. W., X-ray analysis and spectroscopic characterization of M121Q azurin. A copper site model for stellacyanin. *J. Mol. Biol.* **1993,** *229* (4), 1007-21.

26. Lukacs, A.; Eker, A. P. M.; Byrdin, M.; Brettel, K.; Vos, M. H., Electron Hopping through the 15 .ANG. Triple Tryptophan Molecular Wire in DNA Photolyase Occurs within 30 ps. *J. Am. Chem. Soc.* **2008,** *130* (44), 14394-14395.

27. Shih, C.; Museth, A. K.; Abrahamsson, M.; Blanco-Rodriguez, A. M.; Di Bilio, A. J.; Sudhamsu, J.; Crane, B. R.; Ronayne, K. L.; Towrie, M.; Vlcek, A., Jr.; Richards, J. H.; Winkler, J. R.; Gray, H. B., Tryptophan-Accelerated Electron Flow Through Proteins. *Science* **2008,** *320* (5884), 1760-1762.

28. Dodd, F. E.; Hasnain, S. S.; Abraham, Z. H. L.; Eady, R. R.; Smith, B. E., Structures of a blue-copper nitrite reductase and its substrate-bound complex. *Acta Crystallogr., Sect. D: Biol. Crystallogr.* **1997,** *D53* (4), 406-418.

29. Chang, T. K.; Iverson, S. A.; Rodrigues, C. G.; Kiser, C. N.; Lew, A. Y. C.; Germanas, J. P.; Richards, J. H., Gene Synthesis, Expression, and Mutagenesis Of the Blue Copper Proteins Azurin and Plastocyanin. *Proc. Natl. Acad. Sci. U.S.A.* **1991,** *88* (4), 1325-1329.

30. Nilges, M. J., *SIMPOW6, EPR simulation program obtained from the Illinois EPR Research Center (IERC), University of Illinois, U.-C.*

31. Berry, S. M.; Gieselman, M. D.; Nilges, M. J.; Van der Donk, W. A.; Lu, Y., An Engineered Azurin Variant Containing a Selenocysteine Copper Ligand. *J. Am. Chem. Soc.* **2002,** *124* (10), 2084-2085.

32. Ralle, M.; Berry, S. M.; Nilges, M. J.; Gieselman, M. D.; Van der Donk, W. A.; Lu, Y.; Blackburn, N. J., The Selenocysteine-Substituted Blue Copper Center: Spectroscopic Investigations of Cys112SeCys Pseudomonas aeruginosa Azurin. *J. Am. Chem. Soc.* **2004,** *126* (23), 7244-7256.

33. Indika, P. N.; Bayachou, M., Eliminating absorbing interference using the H-point standard addition method: case of Griess assay in the presence of interferent heme enzymes such as NOS. *Analytical and Bioanalytical Chemistry* **2004,** *379* (7-8), 1055-1061.

34. Solomon, E. I.; Penfield, K. W.; Wilcox, D. E., Active sites in copper proteins. An electronic structure overview. *Struct. Bonding (Berlin)* **1983,** *53*, 1-57.

35. Berry, S. M.; Baker, M. H.; Reardon, N. J., Reduction potential variations in azurin through secondary coordination sphere phenylalanine incorporations. *J. Inorg. Biochem.* **2010,** *104* (10), 1071-1078.

36. Romero, A.; Nar, H.; Huber, R.; Messerschmidt, A.; Kalverda, A. P.; Canters, G. W.; Durley, R.; Mathews, F. S., Crystal structure analysis and refinement at 2.15 .ANG. resolution of amicyanin, a type I blue copper protein, from Thiobacillus versutus. *J. Mol. Biol.* **1994,** *236* (4), 1196-211.

37. Palmer, A. E.; Randall, D. W.; Xu, F.; Solomon, E. I., Spectroscopic Studies and Electronic Structure Description of the High Potential Type 1 Copper Site in Fungal Laccase: Insight into the Effect of the Axial Ligand. *J. Am. Chem. Soc.* **1999,** *121* (30), 7138-7149.

38. Ghosh, S.; Xie, X.; Dey, A.; Sun, Y.; Scholes, C. P.; Solomon, E. I., Thermodynamic equilibrium between blue and green copper sites and the role of the protein in controlling function. *Proc. Natl. Acad. Sci. U.S.A.* **2009,** *106* (13), 4969-4974.

39. Strange, R. W.; Dodd, F. E.; Abraham, H. L.; Grossmann, G.; Bruser, T.; Eady, R. R.; Smith, B. E.; Hasnain, S., The substrate-binding site in Cu nitrite reductase and its similarity to Zn carbonic anhydrase. *Nat. Struct. Biol.* **1995,** *2* (10), 912.

40. Klinman, J., P., The copper-enzyme family of dopamine beta-monooxygenase and peptidylglycine alpha-hydroxylating monooxygenase: resolving the chemical pathway for substrate hydroxylation. *J. Biol. Chem.* **2006,** *281* (6), 3013-6.

41. Prigge, S. T.; Mains, R. E.; Eipper, B. A.; Amzel, L. M., New insights into copper monooxygenases and peptide amidation: structure, mechanism and function. *Cell. Mol. Life Sci.* **2000,** *57* (8/9), 1236-1259.

42. Owen, T. C.; Merkler, D. J., A new proposal for the mechanism of glycine hydroxylation as catalyzed by peptidylglycine α-hydroxylating monooxygenase (PHM). *Med. Hypotheses* **2004,** *62* (3), 392-400.

43. Evans, J. P.; Ahn, K.; Klinman, J. P., Evidence that dioxygen and substrate activation are tightly coupled in dopamine b-monooxygenase: Implications for the reactive oxygen species. *J. Biol. Chem.* **2003,** *278* (50), 49691-49698.

44. Jaron, S.; Blackburn, N. J., Does Superoxide Channel between the Copper Centers in Peptidylglycine Monooxygenase? A New Mechanism Based on Carbon Monoxide Reactivity. *Biochemistry* **1999,** *38* (46), 15086-15096.

45. Suzuki, S.; Kataoka, K.; Yamaguchi, K., Metal Coordination and Mechanism of Multicopper Nitrite Reductase. *Acc. Chem. Res.* **2000,** *33* (10), 728-735.

46. Prigge, S. T.; Kolhekar, A. S.; Eipper, B. A.; Mains, R. E.; Amzel, L. M., Substrate-mediated electron transfer in peptidylglycine a-hydroxylating monooxygenase. *Nat. Struct. Biol.* **1999,** *6* (10), 976-983.

47. Ahn, N.; Klinman, J. P., Mechanism of modulation of dopamine b-monooxygenase by pH and fumarate as deduced from initial rate and primary deuterium isotope effect studies. *Biochemistry* **1983,** *22* (13), 3096-106.

48. Tian, G.; Berry, J. A.; Klinman, J. P., Oxygen-18 kinetic isotope effects in the dopamine beta-monooxygenase reaction: evidence for a new chemical mechanism in non-heme metallomonooxygenases. *Biochemistry* **1994,** *33* (1), 226-34.

49. Francisco, W. A.; Knapp, M. J.; Blackburn, N. J.; Klinman, J. P., Hydrogen Tunneling in Peptidylglycine a-Hydroxylating Monooxygenase. *J. Am. Chem. Soc.* **2002,** *124* (28), 8194-8195.

50. Francisco, W. A.; Blackburn, N. J.; Klinman, J. P., Oxygen and Hydrogen Isotope Effects in an Active Site Tyrosine to Phenylalanine Mutant of Peptidylglycine a-Hydroxylating Monooxygenase: Mechanistic Implications. *Biochemistry* **2003,** *42* (7), 1813-1819.

51. Blackburn, N. J.; Rhames, F. C.; Ralle, M.; Jaron, S., Major changes in copper coordination accompany reduction of peptidylglycine monooxygenase: implications for electron transfer and the catalytic mechanism. *J. Biol. Inorg. Chem.* **2000,** *5* (3), 341-353.

52. Hess, C. R.; McGuirl, M. M.; Klinman, J. P., Mechanism of the Insect Enzyme, Tyramine b-Monooxygenase, Reveals Differences from the Mammalian Enzyme, Dopamine b-Monooxygenase. *J. Biol. Chem.* **2008,** *283* (6), 3042-3049.

53. Roeder, T.; Seifert, M.; Kaehler, C.; Gewecke, M., Tyramine and octopamine: Antagonistic modulators of behavior and metabolism. *Arch. Insect Biochem. Physiol.* **2003,** *54* (1), 1-13.

54. Walters, R. R.; Graham, J. F.; Moore, R. M.; Anderson, D. J., Protein diffusion coefficient measurements by laminar flow analysis: method and applications. *Anal. Biochem.* **1984,** *140* (1), 190-5.